

RESEARCH ARTICLE

10.1002/2017JF004367

Downscaling Changing Coastlines in a Changing Climate: The Hybrid Approach

José Antonio A. Antolínez¹ , A. Brad Murray² , Fernando J. Méndez¹ , Laura J. Moore³ , Graham Farley³, and James Wood²

Key Points:

- A new hybrid methodology allows investigation of coastline response to changing climate forcing
- Methodology shows interannual and interdecadal shifts in regional climate forcing through the last century
- Changes in large-scale shoreline shapes arise from shifts in climate forcing

Supporting Information:

- Supporting Information S1

Correspondence to:

J. A. A. Antolínez,
aantolinezja@unican.es

Citation:

Antolínez, J. A. A., Murray, A. B., Méndez, F. J., Moore, L. J., Farley, G., & Wood, J. (2018). Downscaling changing coastlines in a changing climate: The hybrid approach. *Journal of Geophysical Research: Earth Surface*, 123, 229–251. <https://doi.org/10.1002/2017JF004367>

Received 16 MAY 2017

Accepted 26 DEC 2017

Accepted article online 12 JAN 2018

Published online 11 FEB 2018

¹Departamento de Ciencias y Técnicas del Agua y del Medio Ambiente, E.T.S.I. de Caminos, Canales y Puertos, Universidad de Cantabria. Avda. de los Castros, Santander, Spain, ²Division of Earth and Ocean Sciences, Nicholas School of the Environment, Center for Nonlinear and Complex Systems, Duke University, Durham, NC, USA, ³Department of Geological Sciences, Coastal Environmental Change Laboratory, University of North Carolina, Chapel Hill, NC, USA

Abstract Shifts in the frequency of typical meteorological patterns in an ocean basin, over interannual to decadal time scales, cause shifts in the patterns of wave generation. Therefore, ocean basin-scale climate shifts produce shifts in the wave climates affecting the coastlines of the basin. We present a hybrid methodology for downscaling observed (or predicted) climate shifts into local nearshore wave climates and then into the associated coastline responses. A series of statistical analyses translate observed (or predicted) distributions of meteorological states into the deep water wave climate affecting a coastal region and dynamical modeling combined with statistical analyses transform the deep water wave climate into the nearshore wave climate affecting a particular coastline. Finally, dynamical modeling of coastline evolution hindcasts (or predicts) how coastline shapes respond to climate shifts. As a case study, we downscale from meteorological hindcast in the North Atlantic basin since 1870 to the responses of the shape of the coast of the Carolinas, USA. We test the hindcasts using shoreline change rates calculated from historical shorelines, because shifts in coastline shape equate to changes in the alongshore pattern of shoreline change rates from one historical period to another. Although limited by the availability of historical shorelines (and complicated by historical inlet openings), the observations are consistent with the predicted signal of ocean basin-scale climate change. The hybrid downscaling methodology, applied to the output of global climate models, can be used to help forecast future patterns of shoreline change related to future climate change scenarios.

1. Introduction

Approximately 10% of the world's population lives in the coastal zone below 10 m elevation (Nicholls & Cazenave, 2010), in environments that are among the most dynamic on Earth. Natural processes that shape these environments represent hazards to humans and infrastructure, including both acute storm hazards (e.g., storm surge flooding and storm waves) and chronic shoreline erosion. Earth's climate exhibits cycles, including seasonal, sequencing, and clustering of storm events, and interannual and decadal oscillations of various sorts. These cycles are superimposed on an accelerating background climate change arising from human activities (Intergovernmental Panel on Climate Change, 2013), which could involve shifts in the statistics of climate cycles. All of these climate shifts—the cycles and the trend—will tend to cause shifts in coastline position and plan view shape. This work addresses some of the processes that cause long-term (decadal and longer) changes in shoreline location. Although sea level rise, and related cross-shore sediment transport patterns, leads to long-term shoreline erosion (e.g., Bruun, 1962; Cowell, Stive, Niedoroda, de Vriend, et al., 2003; Cowell, Stive, Niedoroda, Swift, et al., 2003; Moore et al., 2010; Wolinsky & Murray, 2009), here we focus on a different set of processes involving alongshore sediment transport, which also produce long-term, cumulative shoreline change. Here we focus on multiannual to centennial time scales.

Although understanding and modeling the long-term behavior of the coastal landscape remains a significant challenge, during the last two decades coastal researchers have increased their efforts to address middle- and long-term morphodynamic evolution (e.g., French et al., 2016; Stive, 2004). Such efforts have led to more robust models, which, by representing only what are hypothesized to be the most important dynamics, require relatively little computational effort and provide insight into which aspects of coastal behavior are

relevant from a long-term point of view and which are not (“signal” versus “noise”) (de Vriend et al., 1993; Lazarus & Murray, 2007; Murray, 2007). However, using such models to address morphological change on particular coastlines during particular time periods requires accurate forcing data at a level of detail and resolution appropriate for a given model during the long periods scientists are interested (e.g., Antolínez et al., 2016; Camus, Mendez, & Medina, 2011). Waves are the most commonly source of data to use as model forcing. However, buoy or satellite data are limited in time to recent decades. If we want to examine coastline change driven by changes in wave climate over a time scale of decades to centuries, as we do here, buoy or satellite data are not sufficient. In addition, to be of use as model forcing, wave data need to be aggregated/synthesized into a form appropriate for a particular model. Here we present a method for generating (hindcasting or forecasting) wave data over time scales spanning from annual to centennial (“hybrid downscaling”; Camus, Mendez, & Medina, 2011; Camus, Méndez, Losada, et al., 2014; Camus, Menéndez, Méndez, et al., 2014), in a form appropriate for a particular model (the Coastline Evolution Model (CEM); Ashton & Murray, 2006a, 2006b).

This work is made possible by the development of techniques to synthesize local wave conditions given only ocean basin-scale meteorological data—surface pressure fields—which extend back 140 years (from atmospheric reanalysis). Different approaches exist for downscaling from basin-scale atmospheric pressure forcing to local wave conditions. In one end-member approach, daily pressure fields could serve as boundary conditions to force dynamic atmospheric models to generate winds, ocean-atmosphere interaction models would then generate the waves, and nested wave transformation models would then propagate the waves to each shoreline location. However, such “dynamic downscaling” is too computationally expensive in the context of a decadal- to centennial-scale modeling endeavor. In addition, a deterministic sequence of daily wave conditions is not needed when modeling large-scale coastline shape changes (because the time scale for response to changing wave forcing is much longer than days; Thomas et al., 2016). Robinet et al. (2016) propose a statistical model that reproduces the interannual variability of shoreline evolution directly from basin-scale atmospheric forcing, with a similar skill as empirical cross-shore models, which require wave data. In contrast, we use a hybrid statistical and dynamical approach that translates daily surface pressure fields into stochastic local wave distributions—an approach that produces wave climate data appropriate to use as model forcing, and with orders of magnitude smaller computational costs than direct dynamical downscaling would incur. In this application, we synthesize local wave data into the form needed to force the CEM: the angular distribution of wave influences on alongshore sediment flux, defined on an annual time scale, measured at the offshore limit of approximately shore-parallel contours (the base of the “shoreface”).

We use the CEM to investigate changes in coastline shape. The shape of coastal environments is function of wave climate and also of the beach cross-shore profile (Hallermeier, 1980) and planform (Falqués et al., 2000). Plan view coastline shapes, on scales from kilometers to hundreds of kilometers, are functions of the angular distribution of wave influences (“wave climate” hereafter; Ashton et al., 2001, 2002; Ashton & Murray, 2006a, 2006b; Falqués et al., 2017; Idier et al., 2011; Kaergaard & Fredsoe, 2013a, 2013b). This relationship arises from patterns in wave-driven alongshore transport. Gradients in net (e.g., annual) transport drive erosion and accretion. When they take place on scales of kilometers and greater, they arise from coastline shape, which (for a given wave climate) dictates patterns of wave momentum and energy fluxes reaching shore. The gradients in transport, in turn, change coastline shape. From these “morphodynamic” interactions (Murray & Ashton, 2013), different coastline shapes emerge under different wave climates. Shifts in wave climate cause shifts in coastline shape, equating to enhanced erosion in some zones and decreased erosion (or accretion) in others (Moore et al., 2013; Slott et al., 2006).

Moore et al. (2013) identified coastline shape shifts associated with decadal-scale wave climate change recorded in wave buoy and hindcast data (Komar & Allan, 2008). Moore et al. (2013) examined changes along the Carolina coastline in Southeastern United States. This well-studied and economically valuable coastline features large-scale cusped capes with a wavelength of approximately 125 km and a cross-shore excursion of 20 km. Two of the capes (Capes Hatteras and Lookout), with extensive protected regions, are approximately unaffected by human shoreline stabilization. The third (Cape Fear) features extensive stabilized stretches of shoreline (Johnson et al., 2015, identified shifts in the rate that resources have been used to stabilize the shoreline associated with wave climate change). As a case study, we will examine changes in the wave climate affecting the Carolina capes over the past 140 years. We will also examine the associated coastline shape changes, through model hindcasts, and compare the hindcasts to observations of historical shoreline change rates (to the extent that available shoreline observations allow).

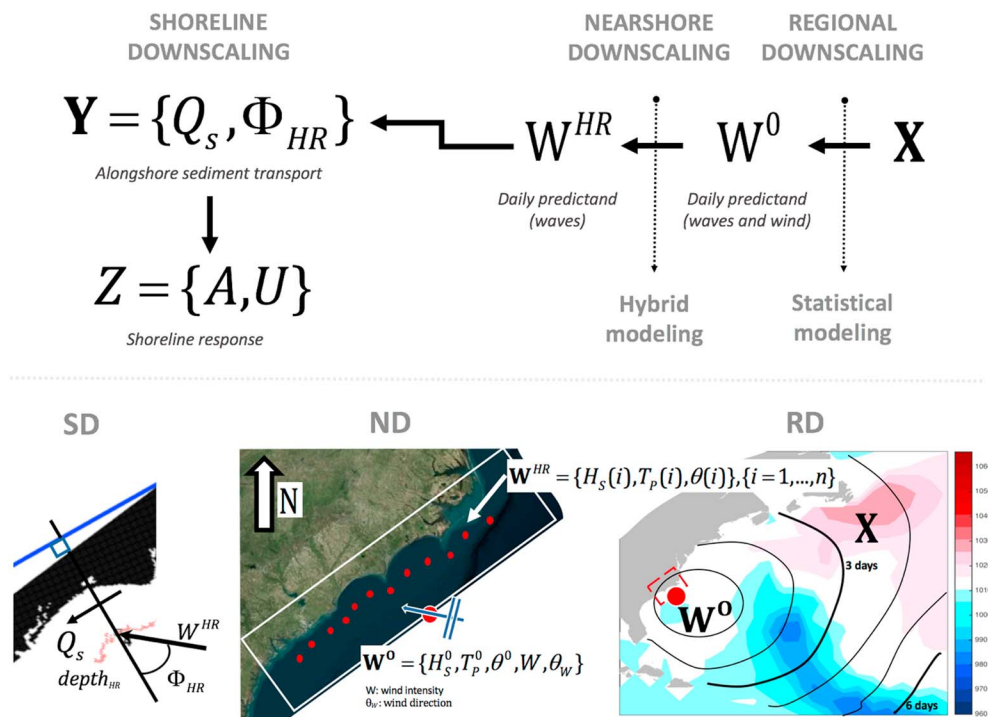


Figure 1. Conceptual framework of the proposed methodology. RD: regional downscaling/ND: nearshore downscaling/SD: shoreline downscaling.

The paper is organized as a sequence of successive steps to be performed to downscale, from the climate, to the shoreline response (see Figure 1). In the supporting information we describe the data used in this work. Section 2 defines a global overview of the methodology, and section 3 explains in more detail the hybrid framework, including the coastline change modeling. In section 4 we compare the hindcast shoreline change rates with historical observations during select periods of time. We summarize conclusions in section 6.

2. Overview of the Methodology

Our approach starts with an empirical distillation of the pressure fields into characteristic daily weather types (DWTs) representing typical patterns of low and high pressure systems and their temporal evolution. Then, taking the time lags associated with wave propagation across the basin into account, a separate statistical step relates the DWTs with typical deep water wave characteristics (sea state type, SST) and wind conditions affecting a target region. To translate these typical SSTs into wave conditions affecting specific coastal locations, we use a dynamical model that propagates the waves in the SST across continental shelf bathymetry and around any obstructions, taking local wind conditions into account. This versatile “hybrid” downscaling approach, mixing statistical and dynamical modeling, can be used to generate wave data with a range of different temporal resolutions, and the wave and wind data can be converted to other forcing variables, including total water level (Rueda et al., 2017). This approach could also be used to address future wave climate change, using the meteorological conditions output from global climate models (Perez et al., 2015). In this initial work, to assess the large-scale and long-term coastline response to interannual and interdecadal shifts in the climate forcing, we synthesize the wave data into a form appropriate for driving the CEM and address past changes along the Carolina Coast.

Figure 1 depicts the three downscaling models we use and the work flow chart. First, a regional downscaling (RD) detects the statistical relationship between the basin-scale atmospheric/oceanic patterns (predictor, X) and the regional deep water wave and wind climate (predictand, W^0) as proposed by Camus, Menéndez, Méndez, et al. (2014). Second, a nearshore hybrid downscaling model (ND; Camus, Mendez, & Medina, 2011) propagates regional waves across the continental shelf, accounting for local winds (predictor, W^0), to obtain high-resolution waves (predictand, W^{HR}) at a depth relevant to the shoreline change modeling (Y): the depth beyond which, in the long-term, wave-driven sediment transport becomes negligible, that is, the base

of the shoreface. The shoreline change modeling requires the following forcing variables: the alongshore sediment transport, Q_s , resulting from waves approaching from each offshore angle, Φ_{HR} (discretized into wave-angle bins, where Φ_{HR} refers to the angle between the wave crests and the local shoreline orientation, measured at the base of the shoreface). We label this sediment transport contribution Y , and we label the distribution of these contributions as a function of the approach angle $f_Y(y)$. As described below, the shoreline modeling (Ashton & Murray, 2006a) uses an empirical formulation for alongshore sediment transport, and Y is integrated as in Ashton and Murray (2006b) to predict the large-scale shoreline response in the long term (Z). The local coastline evolution Z is ultimately driven by changes in the basin-scale atmospheric/oceanic patterns X ; thus, we refer to the shoreline modeling as shoreline downscaling (SD), the third downscaling model. Below we summarize the methodology by describing briefly the different steps through the RD, the ND, and the SD nomenclature.

Step RD1. To define areas of wave generation and characteristic temporal lags of wave energy using ESTELA (Pérez et al., 2014) and to use this information to construct a spatially and temporally varying daily predictor, that is, based on daily sea level pressure (SLP) fields accounting for the temporal lags arising from wave propagation across the domain, as in Hegermiller et al. (2017).

Step RD2. To apply principal component analysis (PCA) to the preprocessed data above (Camus, Méndez, Losada, et al., 2014).

Step RD3. To define DWTs from PCA space of SLP to obtain synoptic SLP patterns (Camus, Menéndez, Méndez, et al., 2014) based on ESTELA (Hegermiller et al., 2017; Pérez et al., 2014). The DWTs are the predictor data (X) of the RD.

Step RD4. To define daily SST performing a classification (Camus, Mendez, Medina, & Cofiño, 2011) on the offshore wave and wind climate. Here the multivariate wave climate distribution for each SST is retained. The SSTs are the predictand data (W^0) of the RD and the predictor data of the ND.

Step RD5. To obtain the categorical distribution of SST for each DWT, $f_{W^0}(w^0)$.

Step RD6. To obtain the monthly distribution of DWT for every year, $f_X(x_t)$.

Step ND1. Selection of daily wave and wind conditions from the offshore wave and wind climate to reduce the number of wave conditions to propagate dynamically, based on Camus, Mendez, Medina, and Cofiño (2011).

Step ND2. HR propagation of the selected cases in step ND1 using SWAN (Booij et al., 1999) accounting for local winds.

Step ND3. Reconstruction of continuous propagated series applying radial basis functions, previously fitted to the continuous daily wave climate series at an offshore location, on the propagated conditions in step ND2. Steps ND1, ND2, and ND3 follow the methodology proposed by Camus, Mendez, and Medina (2011).

Step ND4. To obtain propagated daily SST distributions, predictand of the ND (W^{HR}), and predictor of the alongshore sediment transport, by projecting the propagated series in Step ND3 within each SST defined in Step RD4.

Step SD1. To define the directional alongshore sediment transport distribution, $f_Y(y)$, from the propagated properties of the wave climate (W^{HR}). For each SST, Y is function of a directional discretization (Φ_{HR}) of the alongshore sediment flux (Q_s) following Ashton and Murray (2006b). The direct effect of local winds on alongshore currents and sediment flux is neglected, because forces arising from breaking waves are typically much larger than those arising from local wind drag on the water surface (Fredsoe & Deigaard, 1992).

Step SD2. To integrate the decadal and yearly asymmetry (A) and instability (U) parameters (Ashton & Murray, 2006b) from the combination of the monthly distribution of DWT for every year ($f_X(x_t)$) from Step RD6, the categorical distribution of SST for each DWT from Step RD5 ($f_{W^0}(w^0)$), and the directional alongshore sediment transport distribution ($f_Y(y)$) for each SST from Step SD1.

Note that looking for the relationship between ocean basin meteorological patterns (X) and nearshore waves (W^{HR}), we step into an intermediate stage—the offshore waves and wind (W^0)—because this half step keeps clean the statistical relationship between atmosphere and wave patterns in the study site without adding the effects of shallow-water wave propagation (shoaling, refraction, bottom friction, breaking, ...), which is a function of the bathymetry and makes the search for relationships linking X and W^{HR} more difficult

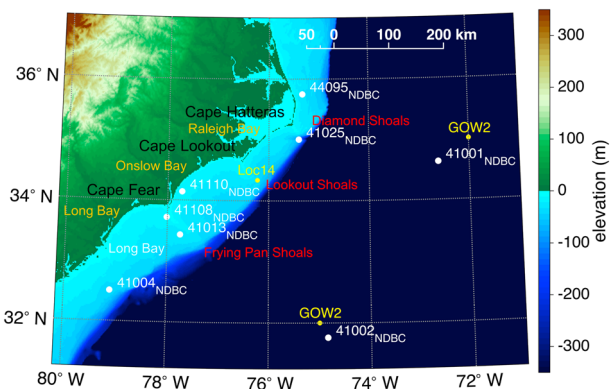


Figure 2. Mosaic of the study site. U.S. East Coast showing the capes and shoals along North and South Carolina. White dots show the location of NDBC buoys. Yellow dots are the location of the offshore hindcast (GOW2) and one of the nodes from the nearshore propagation (Loc14).

because it mixes wave climates from different atmospheric conditions into the same nearshore waves; allows us to independently assess the performance of the individual methods—RD or ND—; and allows for future improvement in the RD or ND methods without repeating everything from scratch.

3. Application

We apply this methodology to the “Carolina capes” of North Carolina and South Carolina, USA (Figure 2).

3.1. Regional Downscaling Model

3.1.1. Predictor Definition

We define the predictor X taking the daily SLP fields from atmospheric reanalysis data (details in Data Set S1 in the supporting information) and combining four different techniques to process the data until the predictor is appropriately optimized. First, we obtain the spatial domain and temporal coverage for the predictor, and then we apply two data mining

techniques: a PCA reducing the data dimensionality and simplifying the subsequent process of classifying the daily atmospheric conditions (using K-means algorithm) into a set of regional synoptic atmospheric patterns related to the regional deep water wave conditions at our location.

Step RD1. Building up the raw predictor data. First, we apply the Estela method (ESTELA; Pérez et al., 2014) on the Atlantic Ocean for the Carolinas coastline based on the historical wave fields. The ESTELA accounts for the source and travel time of the wave energy (regionally generated) reaching our local area. Figure 3 shows that there are three main sources of energy: a northwest, a southwest, and a local one. In line with previous works (Antolínez et al., 2016; Camus, Menéndez, Méndez, et al., 2014) we use daily mean SLP and squared SLP gradient (SLPG) fields from 1872 to 2010 at 2° spatial resolution from the 20CR reanalysis, representing the geostrophic wind conditions over the spatial domain covered by the ESTELA (the envelope of the colormap in Figure 3). As in Hegermiller et al. (2017) we build up the predictor P_t from the SLP and SLPG by accounting for the isochrones (characteristic travel time of the wave energy to the target area, the gray and black lines in Figure 3),

$$P_t(x, t) = [\text{SLP}_{\Omega_1, t}; \text{SLPG}_{\Omega_1, t}; \dots; \text{SLP}_{\Omega_i, t-i+1}; \text{SLPG}_{\Omega_i, t-i+1}; \dots; \text{SLP}_{\Omega_i, t-l+1}; \text{SLPG}_{\Omega_i, t-l+1}] \quad \forall i = 1, \dots, l, \quad (1)$$

where x is the spatial domain, t is time, Ω_i is the domain between daily isochrones $i-1$ and i , and l is the number of days for the longest wave propagation time from generation until arrival at the target location (20 days in this work). We emphasize that with this approach we keep track of the geostrophic wind conditions that generate waves affecting the target location.

Step RD2. Principal component analysis. The raw predictor data P_t at this point are spatial and temporal SLP and SLPG fields spanning the North and South Atlantic Ocean for 139 years at 2° spatial resolution and daily temporal scale. We perform a PCA of P_t to obtain the dominant spatial variability patterns (Empirical Orthogonal Functions, EOFs) and their corresponding temporal coefficients (PCs) (Camus, Méndez, Losada, et al., 2014) reducing the dimensionality (2,478 grid cells for each SLP and SLPG) of the temporal P_t (50,769 days) while preserving the maximum variance of the sample data. We select the first 188 modes from the PCA analysis (explaining 95% of the variance). As an example, the time series associated with the first mode $EOF_1(x)$ is $PC_1(t)$. The original predictor P_t can be expressed as a linear combination of EOFs and PCs:

$$P_t(x, t) = \sum_{i=1}^N EOF_i(x) * PC_i(t). \quad (2)$$

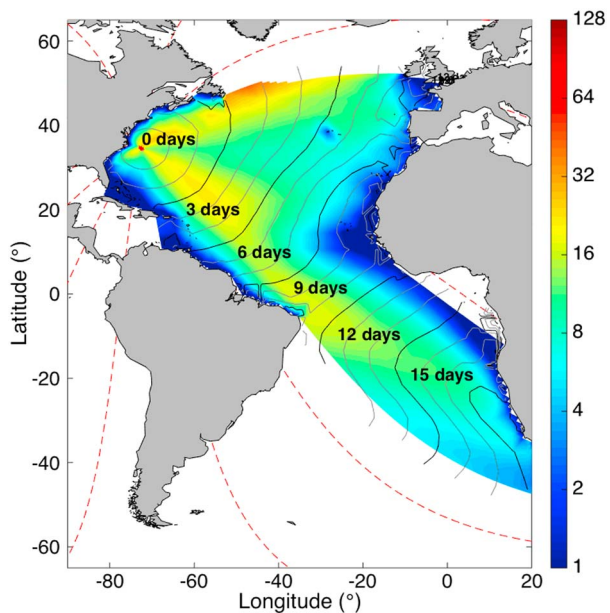


Figure 3. ESTELA applied to the study area. The color map represents the mean effective energy flux from 1993 to 2012 ($\frac{\text{kW}}{\text{m}^2} * 360$), and the gray and black lines represent the characteristic travel time (isochrones). Red lines are the great circles for certain directional sectors.

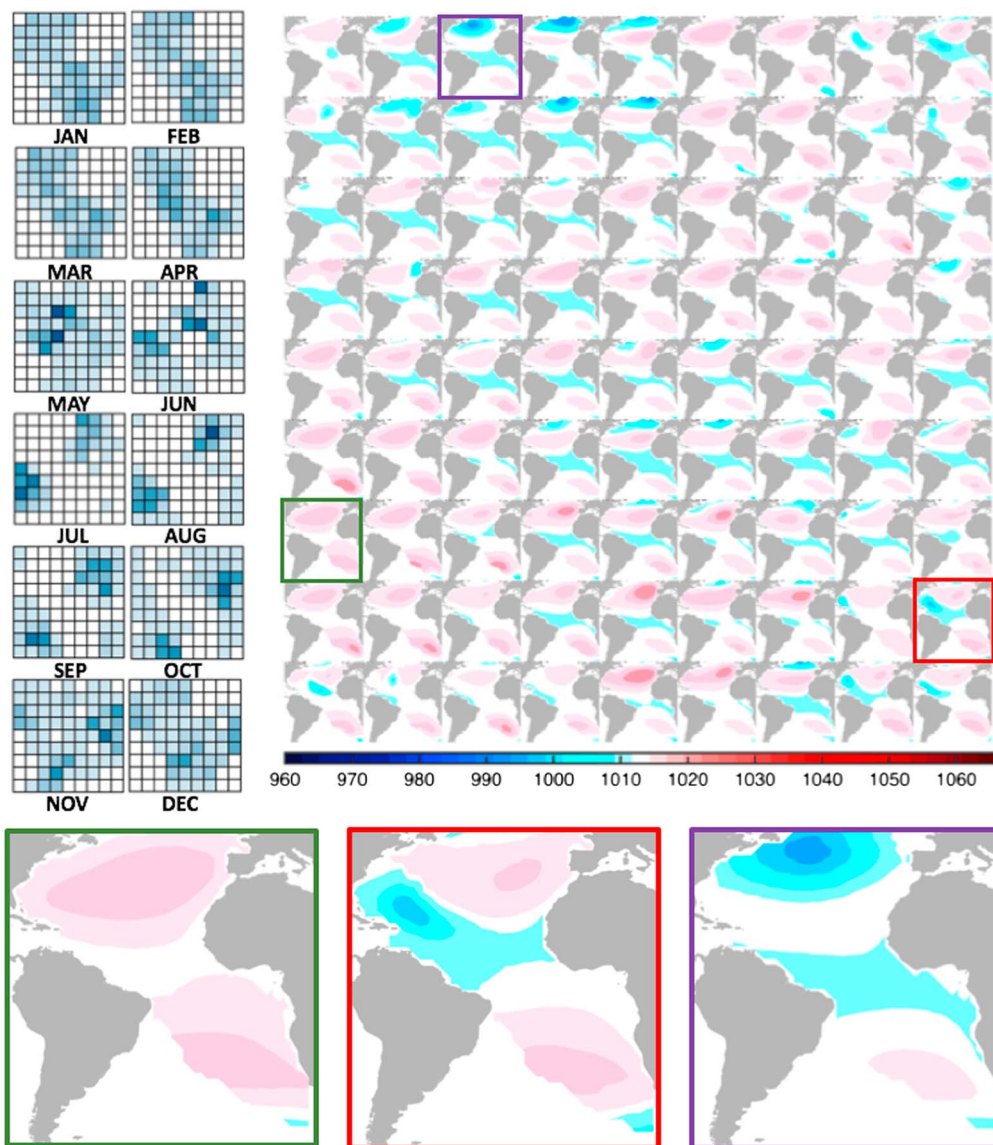


Figure 4. Predictor X. DWT lattice and different weather type patterns: Boreal summer in green (DWT 7), boreal winter in purple (DWT 19), and TC activity in red (DWT 80). The blue-white-red color scale refers to the SLP in hectopascal (hPa). The left panels show the total monthly DWT probability.

Retaining a higher number of modes here than is typical in PCA applications (Antolínez et al., 2016) is a consequence of the high variability introduced by building up the P_t accounting for the ESTELA. At this step, the cubic root of the daily and monthly wave energy flux is regressed from the PCs as in Camus, Méndez, Losada, et al. (2014) to validate the performance of the raw predictor P_t defined above before going ahead with the methodology (details on the preliminary validation of the predictor skill are given in Text S1 in the supporting information).

Step RD3. DWT classification. The preliminary validation model only accounts for linear relationships between waves and the PCs in the time domain. Categorizing the daily atmospheric conditions (statistically summarized by the PCs of P_t) into homogeneous atmospheric circulation patterns allows us to account for nonlinear relationships between waves and the predictor. The link is made in the probability domain (population of multivariate local wave climate related to each homogeneous atmospheric condition) to identify the wave conditions belonging to each weather class or weather type. Following Camus, Menéndez, Méndez, et al. (2014), a K-means classification is applied to the daily PCs space of the raw predictor P_t obtaining $n_{DWT} = 81$, DWTs statistically representative of daily atmospheric synoptic situations. The DWTs are the predictor data X

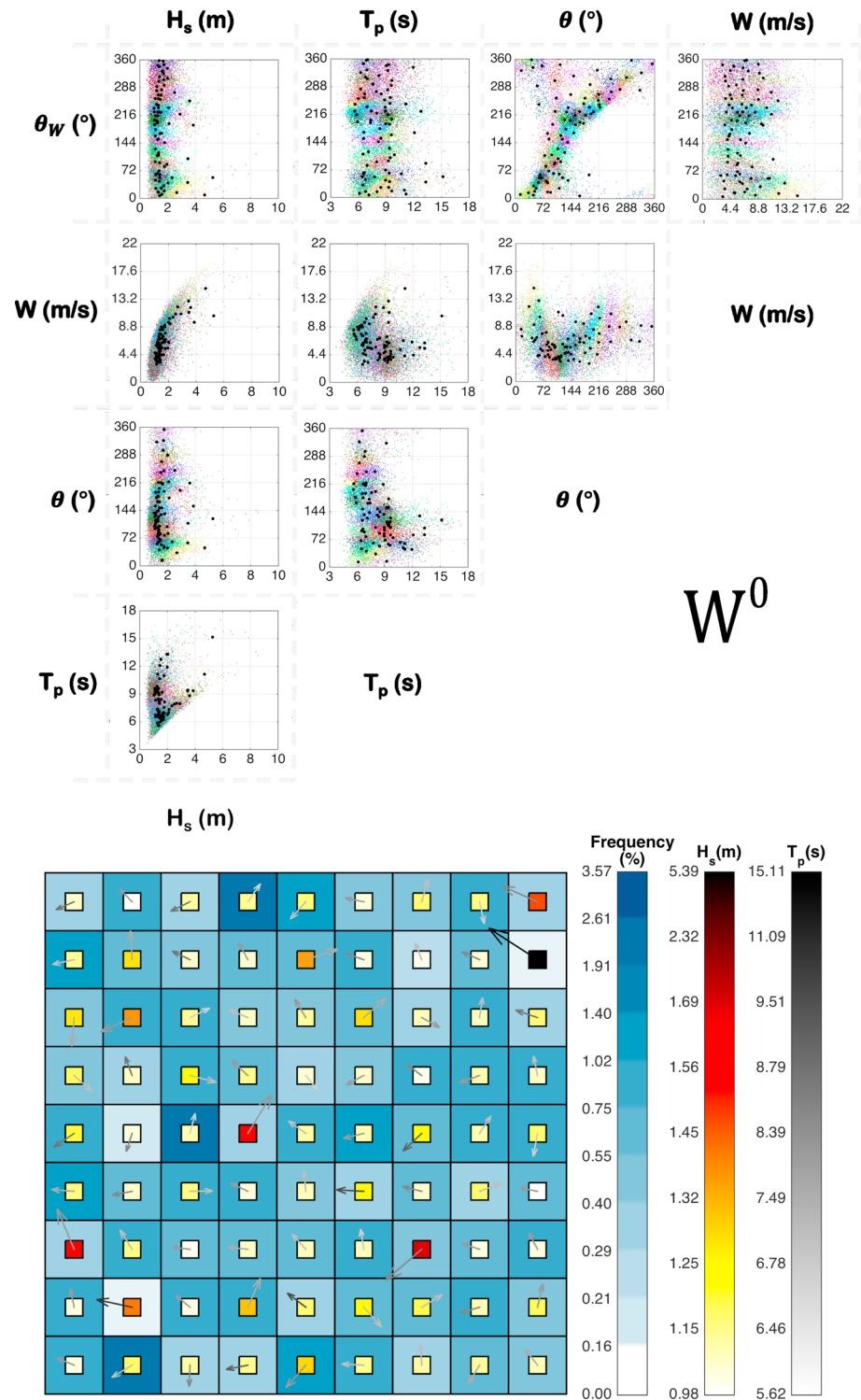


Figure 5. Predictand W^0 . The upper panels show the multivariate classification of wave height (H_s), period (T_p) and mean direction (θ), and wind intensity (W) and direction (θ_W). The different colored dots represent the population within a cluster and the black dots the centroids for each of the 81 clusters. The lower panel shows the centroids projected in a lattice of 9×9 . Blue scale is the occurrence probability for the period of 1979–2014. White-yellow-red-black scale represents the wave height (H_s). The arrow represents the mean direction (θ). The length and gray scale of the arrow represents the period (T_p).

of the RD. Figure 4 shows the lattice of the 81 DWTs arranged with a self-organizing map, producing smooth transitions between adjacent synoptic situations (see Camus, Mendez, Medina, & Cofiño, 2011, for further details on clustering techniques). The left panels represent the total monthly DWT probability; note that there are nine DWTs occurring only during the months of August–October. Even though 20CR does not have enough resolution (2°) to capture the lowest pressures associated with tropical cyclones (TCs), it gets the footprint of very low pressure tracks. The different synoptic patterns are characterized in Figure 4, from boreal winter conditions (December–January–February) feeding southerly winds (e.g., DWT 19 represented in purple), through boreal summer conditions (June–July–August) being related with light northerly winds (e.g., DWT 7 represented in green), to TC activity with strong and highly variable local winds (e.g., DWT 80 represented in red).

3.1.2. Predictand Definition

We define the predictand W^0 from the Global Ocean Waves (GOW2; Perez et al., 2017) data set from 1979 onward for the multivariate wave climate consisting of significant wave height (H_s^0), peak period (T_p^0), and mean direction (θ^0) and the Climate Forecast System Reanalysis U and V components in 10 m height above the sea level to perform the wind intensity (W) and mean direction (θ_w). This data set is extracted at a point (longitude = 72° W, latitude = 35° N) located in deep water close to the buoy NDBC_41001 (see Figure 2). This set of regional deep water multivariate wave and wind climate conditions are the linkage between regional synoptic atmospheric patterns and nearshore waves. Data Sets S1 and S2 in the supporting information contain further details of the data used for the predictand definition, and Text S2 contains more details on the predictand definition.

Step RD4. Daily SST classification. We apply the K-means algorithm technique to daily multivariate time series of the wave and wind climate. Furthermore, we apply the maximum dissimilarity algorithm as a centroid initialization technique to force the K-means technique to correctly describe the high diversity of the daily wave and wind climate (Camus, Mendez, Medina, & Cofiño, 2011). These techniques are applied here to obtain $n_{SST} = 81$ daily SST. Figure 5 shows the classification of the predictand data. Both, n_{DWT} and n_{SST} , were chosen to be a square lattice of $9 \times 9 = 81$ after testing for the highest number of clusters that keep a significant population data on each cluster. In this work, we tried pairs of $\{n_{DWT}, n_{SST}\}$ with $n_{DWT}, n_{SST} = 3 \times 3, 4 \times 4, 5 \times 5, \dots, 10 \times 10$. The SST are the predictand data W^0 of the RD. Note that each daily record of the multivariate wave and wind climate belongs to one of the 81 SSTs. We define the predictand W^0 by

$$W^0 = \{H_s^0, T_p^0, \theta^0, W, \theta_w\}. \quad (3)$$

3.1.3. Statistical Downscaling

We present here the statistical properties of the RD inherited from the statistical relationship between the predictor X and the predictand W^0 .

Step RD5. Monthly distribution of DWTs for every year. The monthly occurrence probability of a DWT for every year is defined as

$$f_X(x_t) = \text{Prob}(\text{DWT} = i / (\text{year} = r \cap \text{month} = s)); \quad (4)$$

$$\forall i = 1, \dots, n_{DWT}; \quad \forall r = 1872, \dots, 2010; \quad \forall s = 1, \dots, 12.$$

We empirically obtain $f_X(x_t)$ from the temporal series of DWT for the period of 1872–2010, defined by $1 \frac{\text{matrix}}{\text{month}} * 12 \frac{\text{month}}{\text{year}} * 139 \text{years} = 1668$ probability matrices of $9 \times 9 = 81$ DWT, represented in the sketch on the left in Figure 6.

Step RD6. Categorical distribution of daily SSTs for each DWT. Here we link the predictand data W^0 to the predictor X ; in other words we project the SST (lower panel of Figure 5) into the DWT lattice (Figure 4). Thus, the probability of the SST “ j ” conditioned to the DWT “ i ” is given by the following:

$$f_{W^0}(w^0) = \text{Prob}(\text{SST} = j / \text{DWT} = i) = \frac{\text{Prob}(\text{SST} = j \cap \text{DWT} = i)}{\text{Prob}(\text{DWT} = i)}; \quad (5)$$

$$\forall j = 1, \dots, n_{SST}; \quad \forall i = 1, \dots, n_{DWT}.$$

We empirically obtain $f_{W^0}(w^0)$ from the temporal series of DWT and SST for the shared period 1979–2010, and it is calculated from the number of SST = j belonging to the DWT = i divided by the total SST belonging to the DWT = i . The right scheme in Figure 6 represents the matrix of matrices.

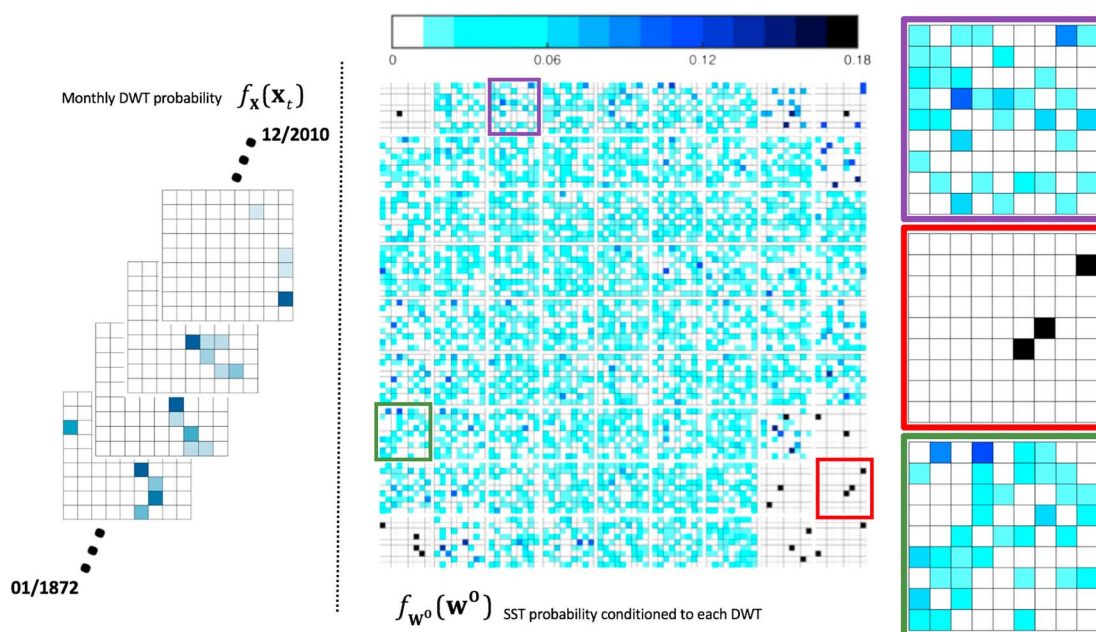


Figure 6. Statistical relationship between the predictor X and the predictand W^0 . The left side shows a sketch of the monthly distribution of DWT, $f_X(x_t)$. The right side shows the categorical distribution of SST for each DWT, $f_{W^0}(w^0)$. We use the same DWT lattice as in Figure 4; however, for $f_{W^0}(w^0)$ within each element of the DWT lattice we represent a lattice of SST. The SST probabilities for different weather type patterns are highlighted: Boreal winter in purple (DWT 19), TC activity in red (DWT 80), and boreal summer in green (DWT 7).

3.2. Nearshore Downscaling Model

The nearshore downscaling model, ND, consists of a dynamical downscaling of the representative subset of SST conditions in deep water, W^0 . The ND output is the propagated distribution function of wave height, period, and direction for each SST defined in section 3.1.2. With the ND we complete the procedure for downscaling local nearshore waves from regional atmospheric conditions, obtaining the likely distribution of the multivariate nearshore wave climate through the twentieth century. Note that this procedure is computationally inexpensive compared with full dynamical downscaling (running wave models continuously in time).

3.2.1. Hybrid Downscaling

Step ND1. Selection of daily wave and wind conditions. First, we apply the maximum dissimilarity algorithm following Camus, Mendez, and Medina (2011) to the daily multivariate time series of wave height, period and direction, and wind intensity and direction described above in section 3.1.2, at the same location, to select $M = 200$ daily sea states to propagate numerically (red dots in top scatters in Figure 7).

Step ND2. Propagation of selected cases using SWAN. Then we perform stationary deep water to nearshore (base of the shoreface) wave transformation of the most representative daily sea states selected above using the wave propagation model SWAN (Booij et al., 1999). The offshore boundary condition of the numerical grid matches the depth at which we take waves from GOW2 reanalysis, indefinite depths (the end of the continental shelf in Figure 2). We define a constant wind field in the computational domain by daily wind intensity (W) and direction (θ_w). Further details of the bathymetry used for propagations are given in Data Set S3 and details of SWAN modeling in Text S3 in the supporting information. The lower panels in Figure 7 show two different wave transformations.

Step ND3. Reconstruction of the continuous propagated multivariate time series. Finally, we carry out the reconstruction of the time series of nearshore wave parameters during the period 1979 to 2014 by an interpolation technique based on radial basis functions, a scheme that is very convenient for scattered and multivariate data (Franke, 1982); details on the use of radial basis functions are in Text S4 in the supporting information. We have validated the reconstructed temporal series against buoy records at different depths. A summary of the results is presented in Table 1. The BIAS in directions is high when the number of data to compare is very low, and/or the difference in depth where the buoy measures against the depth of the closest node

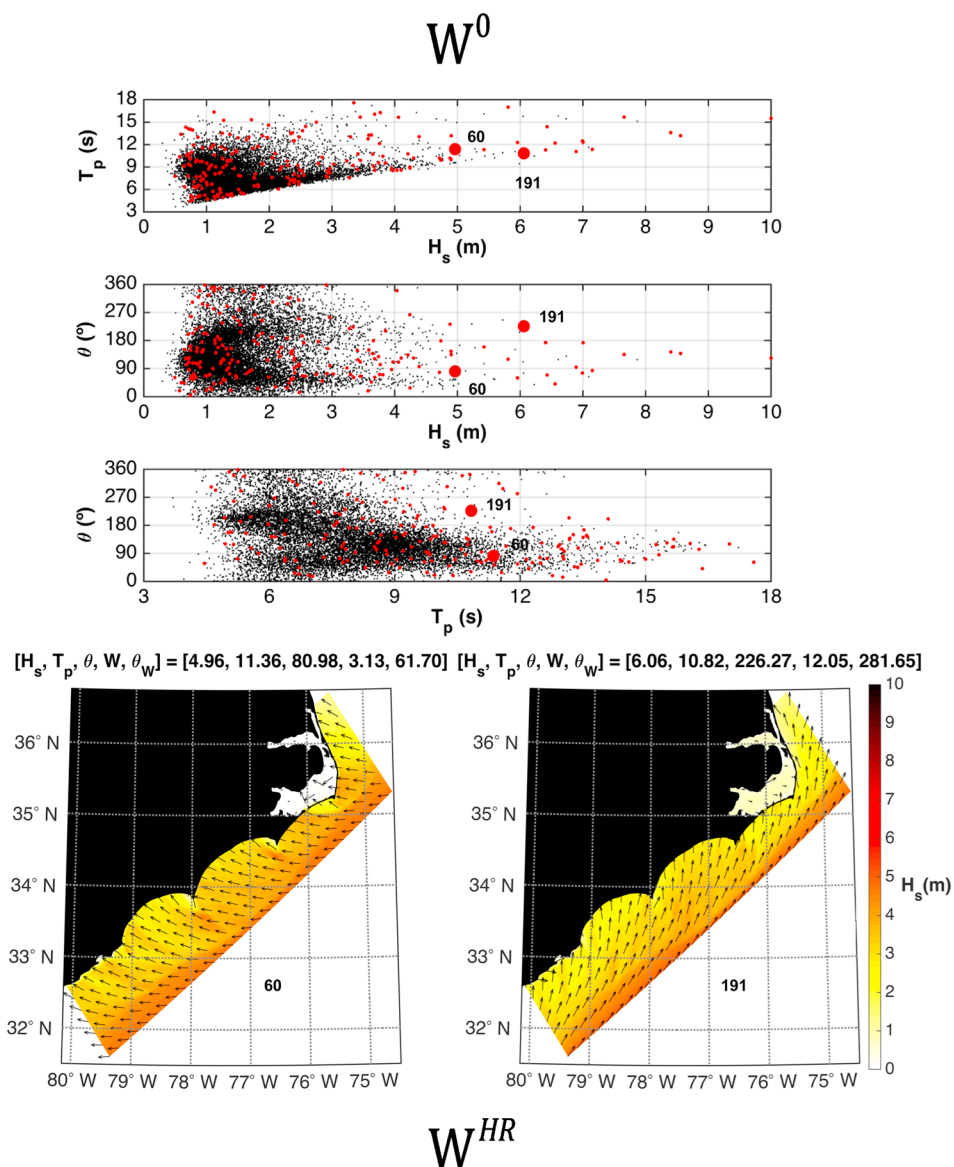


Figure 7. Nearshore wave transformation $W^0 \Rightarrow W^{HR}$. Upper scatters show the 200 selected wave climate conditions (red dots) over the wave climate data (black dots). The lower panels show two representative wave transformations in the computational domain for northern and southern wave direction components. The arrow orientation represents the mean wave direction. The white-yellow-red-black scale represents the wave height. The vectors on top of lower panels are the boundary conditions imposed for each propagation $[H_s(m), T_p(s), \theta(^{\circ}), W(m/s), \theta_W(^{\circ})]$.

Table 1
Comparison of GOW Nodes (G) Against Buoys and Validation of the Hybrid Downscaling (D)

Buoy	Node	Depth (m) buoy/node	Longitude (deg)	Latitude (deg)	Data available	RHO			RMS			BIAS		
						H_s	T_p	θ	H_s (m)	T_p (s)	θ (deg)	H_s (m)	T_p (s)	θ (deg)
NDBC_41001	G	∞	-72.617	34.625	290	0.97	0.88	0.96	0.3	0.97	29.92	-0.01	0.03	15.81
NDBC_41002	G	∞	-74.84	31.76	657	0.97	0.83	0.96	0.22	1.17	27.46	0.01	-0.12	7.03
NDBC_41025	D	68.3 / 105	-75.402	35.006	730	0.77	0.70	0.77	0.56	1.70	52.12	0.07	0.21	23.41
NDBC_41004	D	38.4 / 37	-79.099	32.501	816	0.87	0.79	0.78	0.39	1.42	41.93	-0.08	-0.24	13.92
NDBC_41013	D	23.5 / 28	-77.743	33.436	3,703	0.87	0.77	0.82	0.36	1.52	38.88	0.04	-0.2	6.34
NDBC_44095	D	18.3 / 22	-75.33	35.75	1,214	0.76	0.66	0.59	0.72	2.64	64.02	0.33	0.95	-37.211
NDBC_41110	D	17 / 15	-77.717	34.141	2,552	0.75	0.73	0.61	0.31	2.11	39.24	-0.06	0.22	9.06
NDBC_41108	D	12.8 / 13	-77.743	33.436	944	0.69	0.65	0.76	0.43	2.19	40.88	-0.18	-0.73	-14.73

Note. RHO is the correlation coefficient, RMS is the root-mean-square error, and BIAS is the bias.

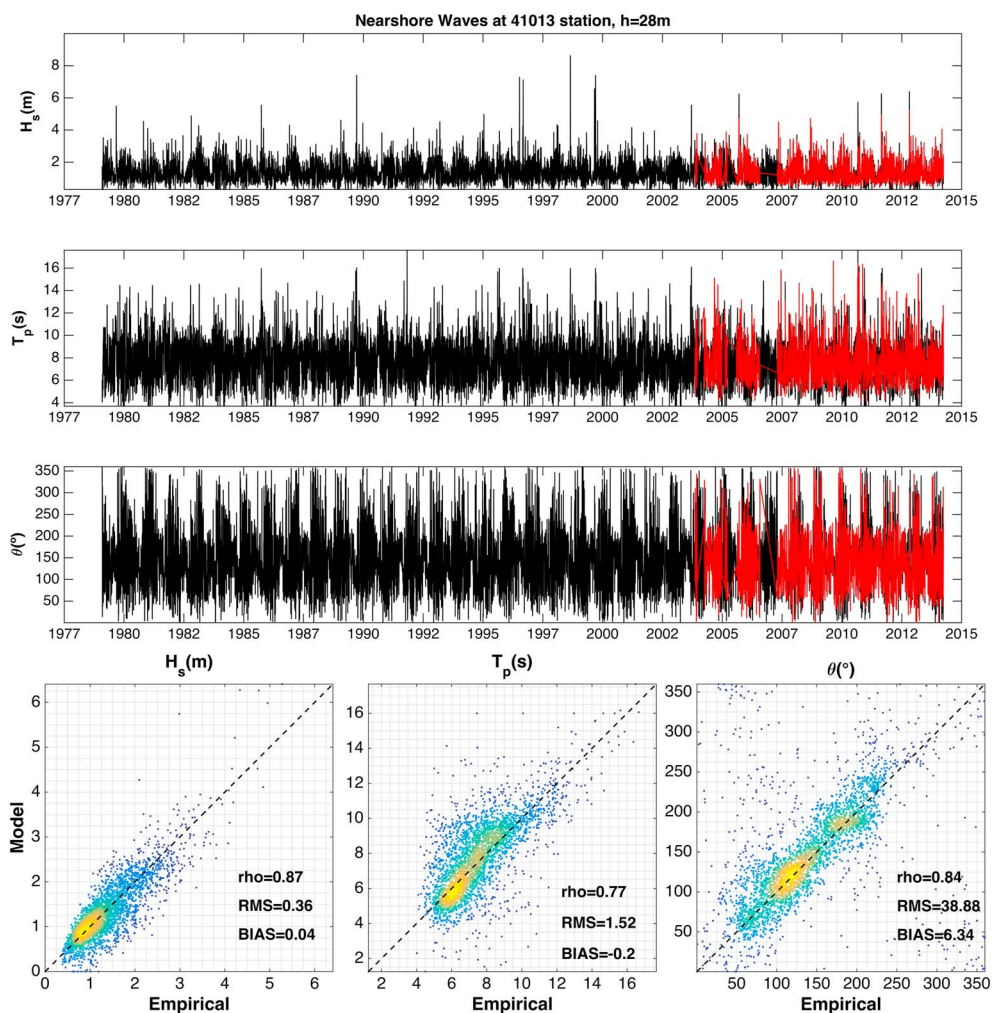


Figure 8. Reconstruction of temporal series. Three upper panels: black lines represent the downscaled time series in the period 1979–2014 and red lines the measured values at the buoy NDBC_41013 at 28 m depth (Figure 2). Squared lower panels: scatter plots of the downscaled daily wave climate (model) against the daily buoy record (Buoy NDBC_41013, empirical). The color map of the scatters represents the density of points, yellow is the maximum density, and blue the minimum. ρ is the correlation coefficient, and RMS is the root-mean-square error.

in the computational domain is significant (e.g., buoy NDBC_41025 is located close to Hatteras Canyon at 68 m depth, but the closest node is at 105 m depth because changes in bathymetry are very strong at this location, Figure 2). Another source of error is the inherited bias from the offshore wave hindcast (see results in NDBC_41001 and NDBC_41002 buoys in Table 1 and the location of the buoys and hindcast nodes in Figure 2). The most valuable comparison is at NDBC_41013 and NDBC_41110 (Figure 2) because there are more than 2,000 daily multivariate wave climate (>5 years); they are centered in the computational grid and the depths in the model and the buoys match sufficiently. We discuss how we address the bias in angle during the shoreline modeling in section 5.

Figure 8 shows the reconstructed series and the quality of the hybrid downscaling at the buoy NDBC_41013 at 28 m depth (location in Figure 2). Note that this methodology supplies continuous temporal series over a longer period than buoys provide and avoids gaps and inhomogeneity in measures.

Step ND4. Categorical distribution of propagated daily SSTs for each DWT. The aim of the hybrid downscaling is to propagate the representative deep water wave and wind conditions to the nearshore. Here we project the daily propagated wave conditions into the lattice of SST defined in section 3.1.2, as each propagated daily

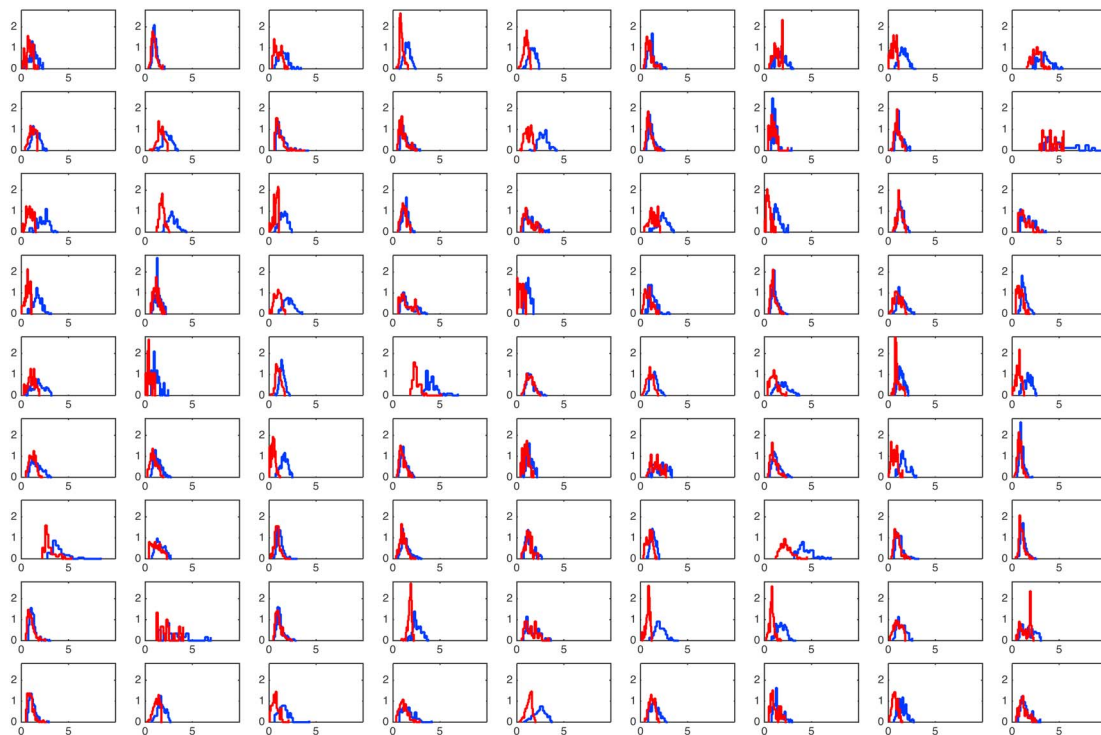


Figure 9. Deep water (blue) and 15 m depth (red) PDFs of significant wave height (H_s) in the SST lattice

wave climate condition is contemporary in time with one SST. The result of this projection is the propagated, HR distribution function of the multivariate wave climate for each SST, W^{HR} :

$$W^{HR} = \{H_S(i), T_p(i), \theta(i)\} \quad \forall i = 1, \dots, n \quad (6)$$

with n referring to the locations where the wave climate has been propagated. Figure 9 shows the deep water and propagated distribution functions of wave height, period, and direction for each SST. The categorical distribution of the propagated SST on each DWT remains constant once the propagated wave climate has been projected to the deep water SST lattice. Thus, we have now captured the statistical relationship between the regional atmospheric conditions X and the nearshore waves W^{HR} relying on the deep water wave and wind conditions W^0 .

$$\begin{aligned} f_{W^{HR}}(w^{HR}) &= f_{W^0}(w^0) = \text{Prob}(\text{SST} = j / \text{DWT} = i) \\ &= \frac{\text{Prob}(\text{SST} = j \cap \text{DWT} = i)}{\text{Prob}(\text{DWT} = i)}; \quad \forall j = 1, \dots, n_{\text{SST}}; \quad \forall i = 1, \dots, n_{\text{DWT}} \end{aligned} \quad (7)$$

3.3. Shoreline Downscaling Model

Waves approaching from “high angles” (angles between offshore wave crests and shoreline orientation larger than the value that maximizes alongshore sediment transport) tend to cause instabilities in coastline shape (Ashton & Murray, 2006a, 2006b; Murray & Ashton, 2013). When the influence of high-angle waves is greater than the influence of low-angle waves (which tend to smooth coastlines), coastlines can self-organize into regular, quasiperiodic shapes similar to those found along many natural coasts at scales ranging from kilometers to hundreds of kilometers. If the asymmetry of the wave climate is small (small net alongshore sediment transport relative to the gross transport), cusped coasts develop that exhibit increasing relative cross-shore amplitude and pointier tips as the proportion of high-angle waves is increased. For asymmetrical wave climates, shoreline features migrate in the downdrift direction. Increasing asymmetrical wave climates produce increasingly asymmetrical coastline features (Ashton & Murray, 2006a). Hence, the SD (1) defines the directional distribution of wave influences on alongshore sediment transport distribution for each SST by applying a simple sediment transport formula and (2) integrates over years and decades the alongshore sediment transport to characterize the asymmetry—the proportion of influence from waves approaching from left, looking offshore (A)—and the proportion of influence from high-angle waves (U) in the effective wave climate over those time scales.

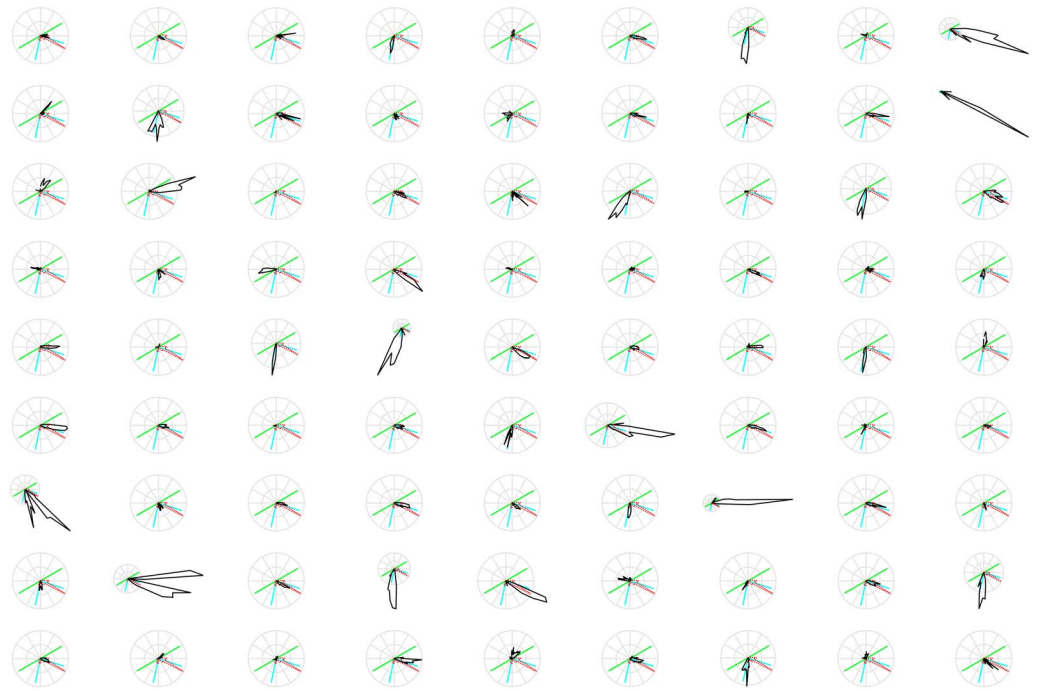


Figure 10. Directional distribution of alongshore sediment transport $f_Y(y)$ in the SST lattice. Green line is the shoreline orientation (N60°E); cyan lines define the reference relative 42° relative angle (at the seaward limit of approximately shore-parallel contours) that maximizes sediment transport (Ashton & Murray, 2006a). Black line is the directional alongshore sediment transport distribution for each SST, $f_Y(y)$, and red line is the average of $f_Y(y)$ for all the SST. Note that in the SST with largest values of directional alongshore sediment transport, $Y(y) = Q_S(\Phi_{HR})$, the circles have been scaled to fit in the lattice but they represent the same magnitude as in the other groups.

Step SD1. Distribution of alongshore sediment transport. In this step we compute the daily alongshore sediment transport from the nearshore wave climate (W^{HR}) applying the CERC sediment transport formula (Komar, 1971). We take the mean coastline orientation to be N60°E (Ashton & Murray, 2006b). Then we achieve the directional alongshore sediment transport distribution for each SST, $f_Y(y)$, partitioning the sediment transport into bins of 5°, where the representative angle of the bin is defined by Φ_{HR} and the accumulated sediment flux value by Q_S . Thus, the directional alongshore sediment transport is given by $Y = Q_S(\Phi_{HR})$ and the directional distribution for each SST by $f_Y(y)$. Figure 10 shows the $f_Y(y)$ obtained with nearshore wave parameters during the period 1979 to 2014 in the location Loc14 in front of Cape Lookout at 30 m water depth (see Figure 2). The lower right panel of Figure 11 shows the sediment transport variables involved in the directional distribution of alongshore sediment transport $f_Y(y)$.

Step SD2. Decadal and yearly A and U parameters. Here we integrate $f_Y(y)$, $f_{W^0}(w^0)$, and $f_X(x_t)$ to calculate the cumulative directional alongshore sediment transport distribution during yearly and decadal time spans, $f_Y(y_t)$, as below:

$$f_Y(y_t) = \sum_{n_{DWT}} \sum_t f_X(x_t) \cdot \sum_{n_{SST}} f_{W^0}(w^0) \cdot f_Y(y). \quad (8)$$

where $\sum_{n_{SST}} f_{W^0}(w^0) \cdot f_Y(y)$ is the cumulative alongshore sediment transport for each DWT, $\sum_t f_X(x_t) \cdot \sum_{n_{SST}} f_{W^0}(w^0) \cdot f_Y(y)$ is the cumulative alongshore sediment transport for each DWT in a period of time t , here a decade or a year, and integrating over the DWT, $\sum_{n_{DWT}}$, accumulates the total $Y_t = Q_{S,t}(\Phi_{HR})$ for each directional bin to obtain $f_Y(y_t)$. The top roses in Figure 11 show the decadal alongshore sediment transport distribution from 1872 to 2010. The decadal roses present two very different directional sediment contributions, a southerly (contribution from the right looking onshore) and a northerly (contribution from the left). These contributions vary through time as is shown by comparing to the mean value for the study period (red dotted line in Figure 11). The end of the nineteenth century is characterized by more asymmetry and more low-angle influence (sediment transport contribution between the two cyan lines in the decadal alongshore sediment transport distribution) in the wave climate. For example, the northerly component in the 1880–1990

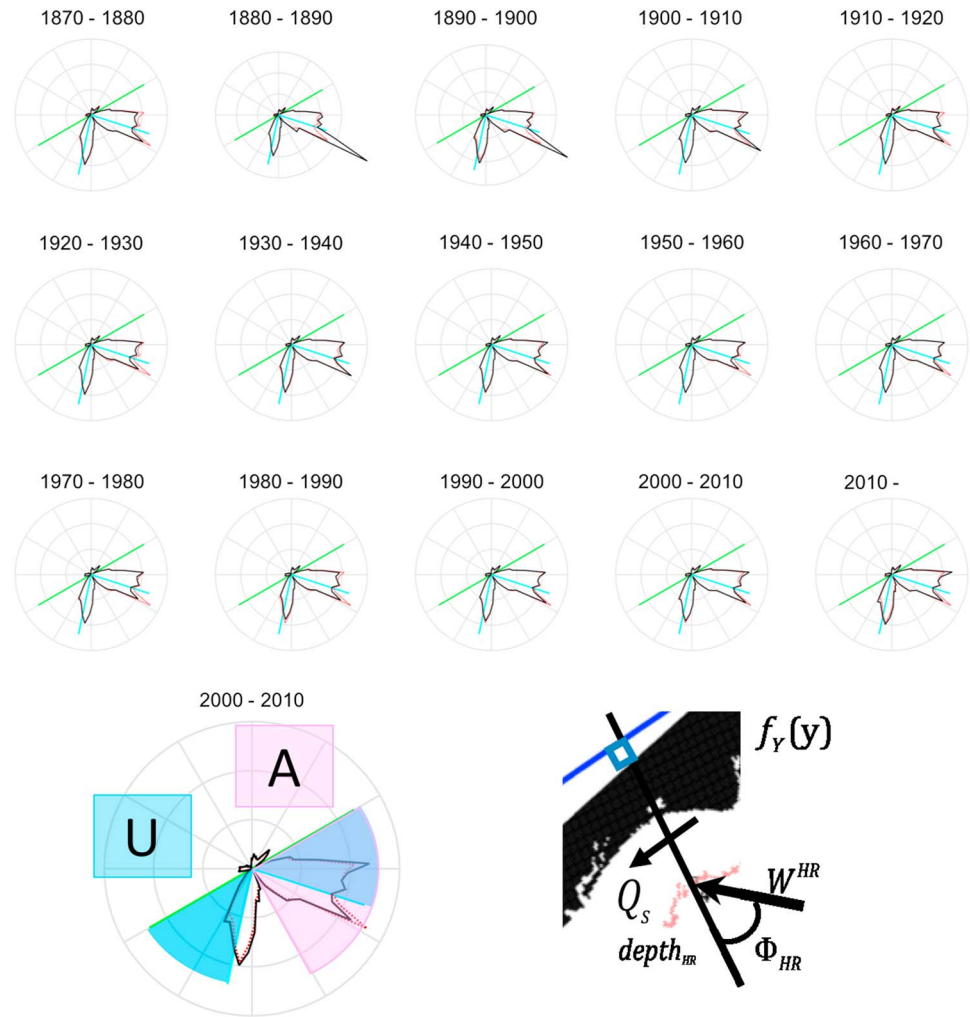


Figure 11. Decadal directional distribution of alongshore sediment transport $f_Y(y_t)$ (upper roses). Green line is the shoreline orientation (N60°E); cyan lines define the reference 42° angle above which a wave tend to cause instability in coastline shape according to Ashton and Murray (2006a, 2006b). Black line is the decadal distribution $Y(y_t)$, and the red line is the mean value for all the decades. The lower left rose shows scheme for the integration of A and U parameters. The lower right scheme shows the sediment transport variables involved in the directional distribution of alongshore sediment transport $f_Y(y)$.

distribution is larger than in the 1910–1920 distribution, relative to the southerly component. Changes in the relative influences on alongshore sediment transport from waves approaching from different directions will be reflected in the migration rate and shape of coastline features (Z).

We integrate the decadal and yearly A and U parameters from $f_Y(y_t) = f_Y(Q_{s,t}(\Phi_{HR}))$ as follows (see also the lower left panel of Figure 11):

$$A = \frac{\int_{\Phi_{HR} > 0} f_Y(Q_{s,t}(\Phi_{HR})) d\Phi_{HR}}{\int_{\forall \Phi_{HR}} f_Y(Q_{s,t}(\Phi_{HR})) d\Phi_{HR}} \quad (9)$$

$$U = \frac{\int_{|\Phi_{HR}| > 42} f_Y(Q_{s,t}(\Phi_{HR})) d\Phi_{HR}}{\int_{\forall \Phi_{HR}} f_Y(Q_{s,t}(\Phi_{HR})) d\Phi_{HR}}, \quad (10)$$

Figure 12 depicts the variability in values of A and U over annual and decadal time scales.

3.4. Downscaled Shorelines

In this section, we drive the CEM (Ashton & Murray, 2006a) using yearly A and U parameters (dotted black line in Figure 12) over the period of 1870–2010. We generate an initial coastline using the values of U

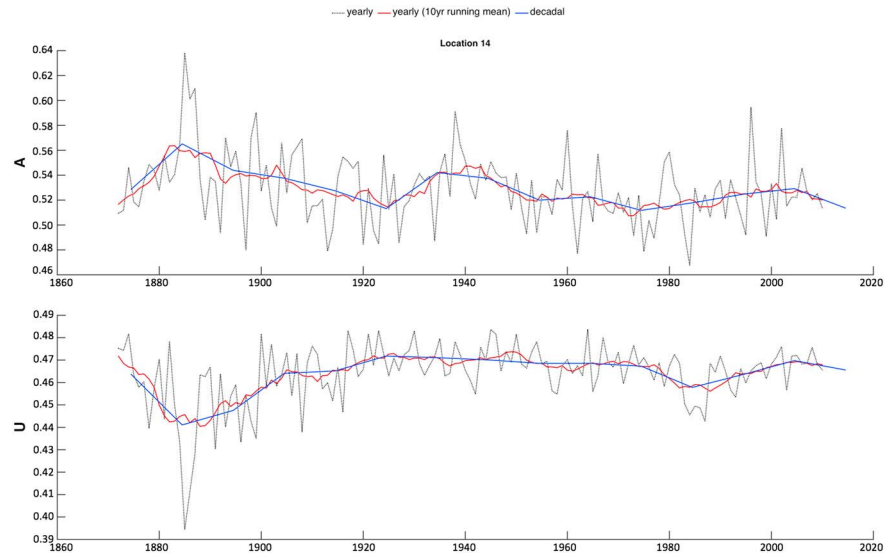


Figure 12. Yearly values (black), 10 year running mean of yearly values (red) and decadal (blue) A and U parameters for the study period in location Loc14.

and A that maximize the resemblance between the model capes and the Carolina capes, $U = 0.6$ and $A = 0.55$ (Moore et al., 2013). Then, to examine the responses of a coastline (Z) with some of the main characteristics of the Carolina Coast to the action of historical (hindcast) wave climate, we vary U and A relative to these mean values using the differences from the mean shown in Figure 12. Figure 13 (right panel) exhibits the values used to force CEM. Figure 13 (middle panel) shows the 10 year running mean of the yearly shoreline

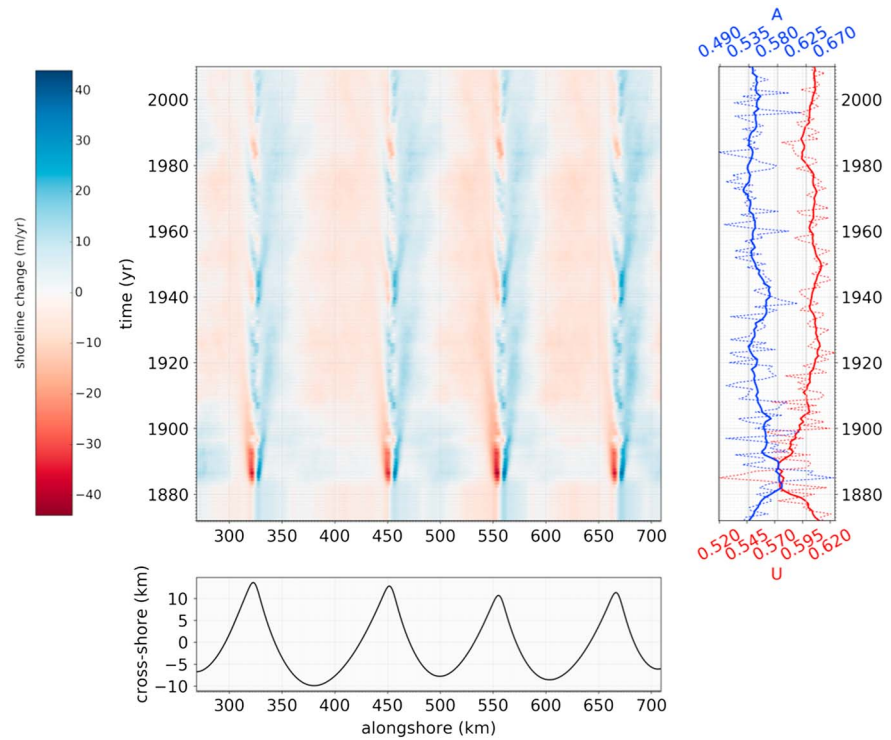


Figure 13. CEM model results. The middle panel shows the 10 year running mean of the yearly shoreline change rate; red is erosion, and blue is accretion. The lower panel is the initial model shoreline with scales resembling the Carolina capes. The right panel shows the yearly values of A and U (dotted lines) and the 10 year running mean of yearly values (continuous lines).

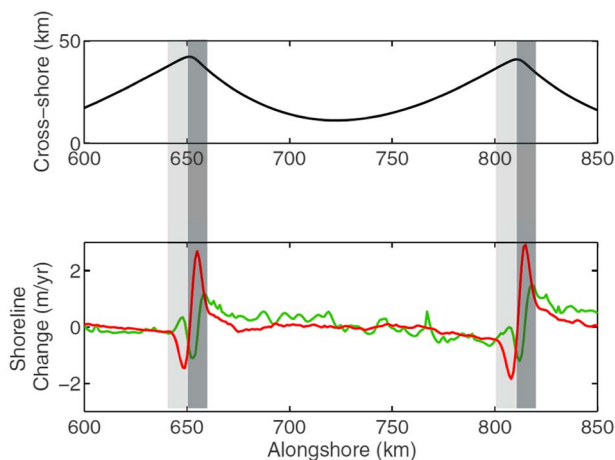


Figure 14. (upper panel) The resulting coastline after forcing with the best fit wave climate (black) and (lower panel) mean shoreline change after 100 years for the best fit climate (green) and for increased summer hurricane waves (red). The darker (lighter) gray regions cover approximately 10 km north (south) of cusp locations (source: Moore et al., 2013).

Model predictions shown in Figure 13 include a strong contrast between the patterns of change before approximately 1908 and during the 1908–1938 period (which we term “period 1” and “period 2,” respectively). We focus on testing whether this strong predicted signal can be detected in historical observations.

But first, we carry out a preliminary assessment of how reliable the predicted signals are, by comparing the model results based on the downscaling presented here to a previous modeling effort based on buoy and

Wave Information Study wave hindcasts for a more recent period, 1974–2004 (Moore et al., 2013). Moore et al. (2013) examined the response of modeled capes to an altered wave climate, with a single pair of altered *A* and *U* values representing the culmination of a trend observed in buoy observations. Figure 14 shows how time-averaged shoreline change rates influenced by wave climate change differ from the rates under a constant wave climate, featuring increased erosion extending approximately 10 km updrift of the cape tips and increased accretion downdrift of the tips. This climate change signal also appears in Figure 13. Although Moore et al. (2013) only looked for a signal representing the period as a whole, Figure 13 features pronounced erosion within 10 km updrift of cape tips in the 1980s and pronounced accretion just downdrift of the tips during the 1990s and early 2000s.

This period, 1974–2004, features not only buoy and Wave Information Study data but also shoreline data—data that are more reliable and more frequent than the shoreline data from the late nineteenth or early twentieth centuries. Therefore, we also compare our predicted model signals with an analysis of shoreline change during this period (Moore et al., 2013). Figure 15 shows the modeled shoreline change rate (top panel) and the observed rates for the flanks of Cape Hatteras (bottom). To assess whether the component of shoreline change from gradients in alongshore transport, driven by downscaled wave climate data, is relevant on natural shorelines, we focus on the areas adjacent to and updrift of Cape Hatteras (excluding the shoreline in the vicinity of Hatteras Inlet, on the downdrift flank, as discussed further below). The rough correspondence between modeled and observed shoreline change rates near and updrift of the cape

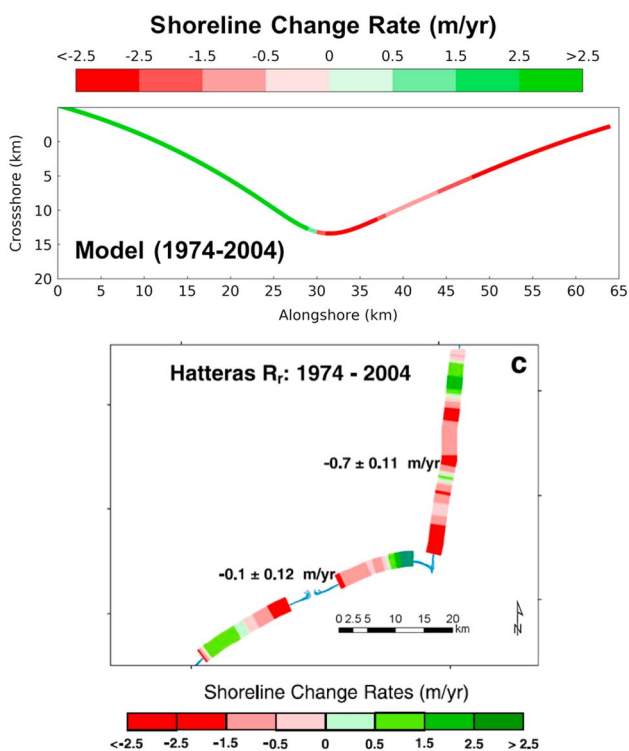


Figure 15. Upper panel: predicted shoreline change rate (m/yr) in the period 1974:2004. Lower panel: measured shoreline change rate (m/yr) in the period 1974:2004 for Cape Hatteras (source: Moore et al., 2013).

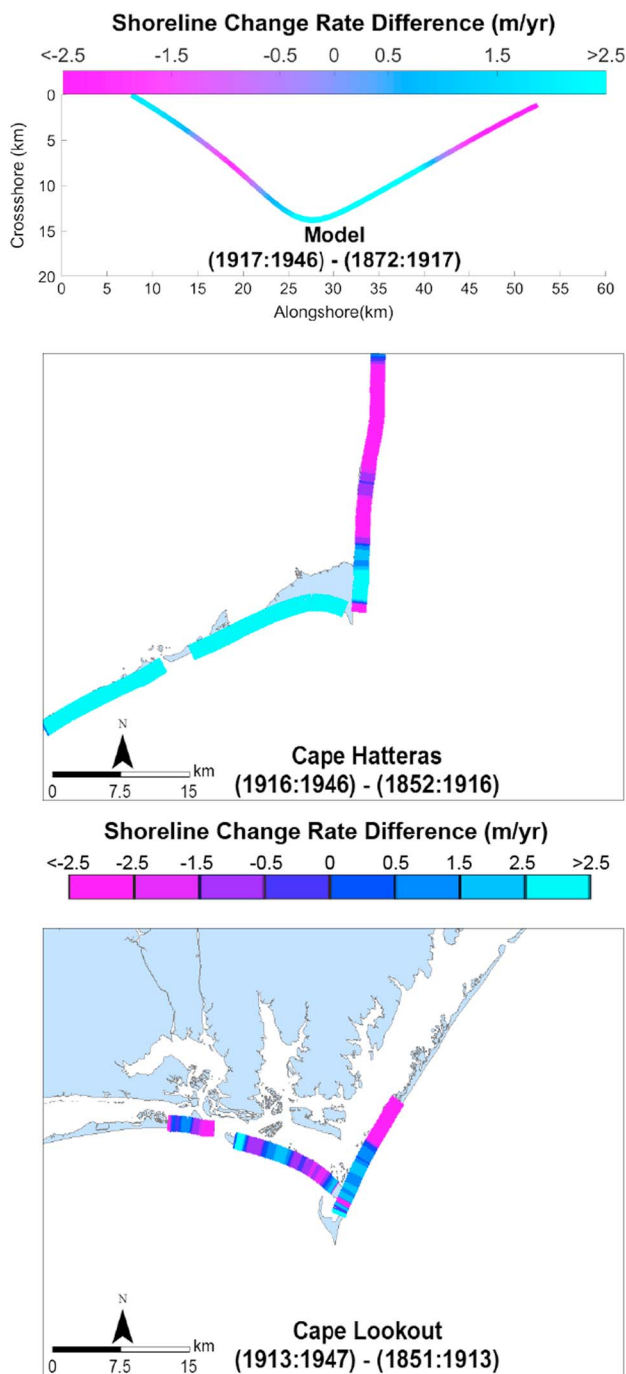


Figure 16. Upper panel: predicted shoreline change rate difference (m/yr) between period 1 (1872:1917) and period 2 (1917:1946). Results are an average of the rates for the capes shown in Figure 13, representing a generic cape with characteristics similar to those of the Carolina capes. Middle panel: measured shoreline change rate difference (m/yr) between period 1 (1852:1916) and period 2 (1916:1946) for Cape Hatteras. Lower panel: measured shoreline change rate difference (m/yr) between period 1 (1851:1913) and period 2 (1913:1947) for Cape Lookout.

tip is consistent with the conclusion that the shoreline change processes represented in hybrid downscaling play a significant role in producing shoreline change on natural coastlines.

Turning back to the period featuring the strong predicted shoreline change signal during the late nineteenth and early twentieth centuries, Figure 16 shows the difference between shoreline change rates calculated for period 1 and period 2 from model results and observations from near Cape Hatteras and Cape Lookout.

Two factors complicate this test. First, the availability of historical meteorological observations differs from the availability of historical shorelines; our model results, based on meteorological data, begin in 1871, while historical shoreline change rates pre-1908 can only be determined between approximately 1850 and approximately 1915. Thus, period 1 includes two decades of shoreline change in the observations that cannot be included in the model results. Second, the opening of inlets during these historical periods affects the shoreline change rates on the downdrift flanks of the capes (to the southwest of the cape tips). The large Hatteras Inlet opened at approximately the beginning of period 1, and the growth of large tidal deltas during period 1 acted as a sediment sink for the surrounding coastlines, driving local patterns of rapid shoreline change. Thus, shoreline change rates became much less erosional in period 2 relative to period 1 on the downdrift flank of Cape Hatteras, for reasons not connected to changes in wave climate. Similarly, Barden Inlet opened downdrift of the tip of Cape Lookout during the period 2, altering coastline change patterns there. (We do not include Cape Fear in this analysis, because dredging of the river channel strongly affects shoreline change rates both updrift and downdrift of the cape tip.)

Therefore, we focus our comparison on the updrift flanks of the capes. We do not compare the absolute rates of change during each period in model results to observations for two reasons: (1) The rates of shoreline change can be adjusted in the model (by adjusting the poorly constrained empirical coefficient in the parameterization for alongshore sediment flux). (2) We are assessing whether the signal of climate change involving altered wave climate and related alterations to alongshore sediment transport gradients has significant roles in past shoreline change patterns, although cross-shore sediment transport, such as the overwash during major storms, also contribute to the magnitude of shoreline change. Rather than comparing raw shoreline change magnitudes, to test for the climate change signal we are addressing, we compare the observed alongshore pattern of differences in shoreline change rates from one period to the other. The model predicts (Figure 16, upper panel) that (1) within approximately 10 km updrift of the cape tips, the trend from period 1 to period 2 should have been toward more accretion/less erosion (positive values of the difference in shoreline change rates between the two periods) and (2) farther updrift, the trend should have been toward less accretion/more erosion. Figure 16, lower panels, shows the changes from one period to the other in the observations, exhibiting a shift toward more accretion/less erosion near the cape tips and toward less accretion/more erosion farther updrift. In addition, the transition from more accretion/less erosion to less accretion/more erosion occurs at a distance updrift of the cape tip on the order of 10 km, roughly matching the spatial scale of the transition in the model results (Figure 16, upper panel).

5. Summary and Discussion

5.1. Model Limitations

We have presented a “hybrid approach,” combining statistical and dynamical modeling, to downscale from meteorological hindcast in the North Atlantic basin since 1870 to the responses of the shape of the coast of the Carolinas, USA. In the first step, RD, we use the daily SLP fields from the ensemble mean of 20CR reanalysis to build up 81 different weather types (X) reproducing the interannual variability through the period of 1872–2010. In this step, we link the offshore wave and wind climate conditions (hindcast) W^0 , with the atmospheric conditions X , in the period of 1979–2010 through a statistical relationship. Here we use empirical distributions although statistical models could be used instead (Antolínez et al., 2016; Méndez et al., 2007; Rueda et al., 2017). This method will statistically reflect any variability presented in X into W^0 . Note that the 20CR data assimilation system is based on an ensemble Kalman filter. The data are produced in a series of 5 year “streams”(independent runs), with 56 members in each stream (Compo et al., 2011). Therefore, ensemble members only remain temporally continuous during the 5 year duration of each stream. This is reflected in how variability is assessed over long time periods. The increased uncertainty in the early period of the data leads to greater disagreement between the ensemble members, such that a time series of their mean will have much less variability than the members individually. This would lead to a spurious strong reduction in variability appearing at earlier times in the ensemble mean.

In the second step, ND, we propagate W^0 —the daily offshore wave conditions accounting for local wind—to the nearshore (W^{HR}) during the period of 1979–2010. We combine 200 SWAN runs of multivariate wave and local wind conditions in the hindcast period, selected with data mining techniques (maximum dissimilarity algorithm), with statistical interpolation techniques (radial basis functions) to reconstruct the daily continuous temporal series in the nearshore. Tests reveal that increasing the number of runs does not improve the results significantly. We could increase the complexity of the nearshore wave propagation by forcing spatial wave and wind fields instead of uniform multivariate wave and wind climate at the offshore boundary. However, as forcing for the CEM, increasing the spatial resolution of the nearshore wave data would not be useful. Furthermore, we could account for temporal changes in bathymetry if multiple bathymetries were available. With the procedure we have used, any variability presented in X will be statistically reflected in W^0 and so in W^{HR} .

The CEM omits several factors and processes that contribute to changes on natural coastlines. In this work, we do not consider alongshore variations in underlying lithology (Moore et al., 2010; Valvo et al., 2006), and in the coastline modeling we do not consider local variations in wave conditions arising from complicated nearshore bathymetry (Limber et al., 2017; McNinch, 2004; Schupp et al., 2006). (The downscaled nearshore wave data include local variations at depths that can extend to the limit of wave breaking, but to force the CEM, we use only the wave data at depths corresponding to the base of the shoreface, and we average different locations alongshore.) In such a “one-contour-line model,” coastline accretion or erosion arises from gradients in net alongshore sediment transport that occur in the uppermost portion of the shoreface profile, and the accretion or erosion is distributed across the whole shoreface all at once. This simplified approach neglects delays in propagating the accretion or erosion to the lower parts of the shoreface profile (Kinsela & Cowell, 2015), which over the time scales of decades can alter the rates of coastline response to alongshore transport gradients. Thus, when comparing modeled to observed shoreline change rates, we emphasize not the magnitude of the rate but rather the patterns of alongshore variations in the rates, which are diagnostic of the climate change signals we are testing for (Figure 16).

Perhaps most notably, one-contour-line models do not address the component of shoreline erosion that arises from cross-shore sediment fluxes shoreward of the beach. Strong storms wash sediment from the beach and upper shoreface landward. Such “overwash” events remove sand from the beach and shoreface, inducing shoreline erosion. And because the frequency and magnitude of such events tends to increase with the rate of sea level rise, the resulting component of shoreline change is related to the rate of sea level rise. The model results presented here do not include this component of shoreline change, but neither other cross-shore processes. With the simplifying assumption that the sea-level-rise-related component of shoreline changes is approximately homogeneous alongshore, that component could be superimposed with the CEM results presented here. However, the alongshore variations in shoreline change rates we are using to test for the signals of wave climate change would be unaffected. On the other hand, the cross-shore sediment fluxes that arise from the opening of an inlet and the subsequent growth of ebb- and flood-tidal deltas contribute a strong shoreline change signal that is alongshore heterogeneous. This signal complicates the detection of the wave

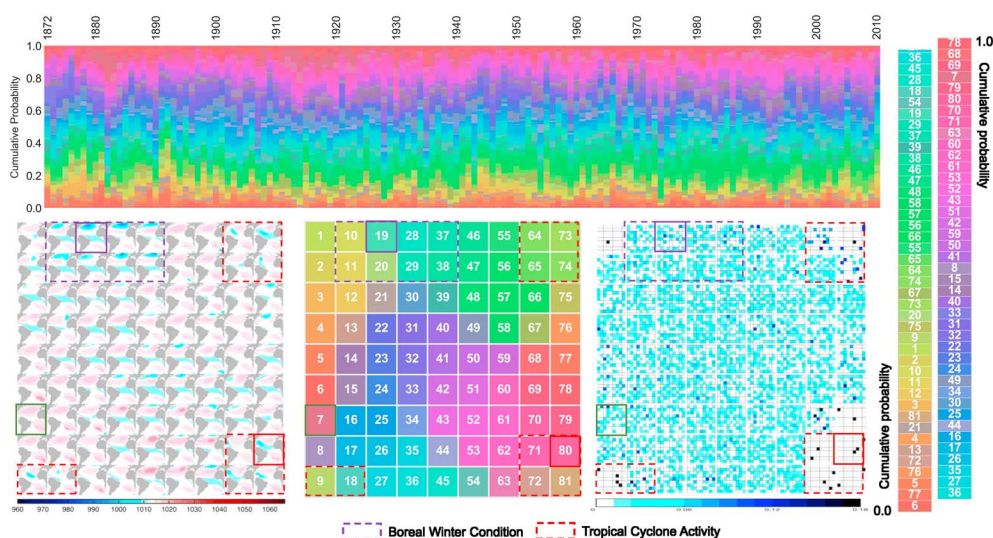


Figure 17. Interannual variability of the DWTs (X). Upper panel: yearly occurrence probability for the 81 DWTs. Lower left panel: DWT lattice as presented in Figure 4. Lower middle panel: self-organizing map of the colors used in the upper panel with the same organization as the DWT in the lower left panel. Lower right panel: categorical distribution of SST for each DWT. The right side color bar represents the numbers and colors of the DWT in lower middle panel with the same order than in the upper panel. It links the lower left and right panel with the upper panel.

climate change signal we are testing for, prompting us to exclude the portions of the coastline in the vicinity of inlets from the comparisons between model hindcasts and historical observations.

The processes and factors omitted in the CEM would be flaws in a model designed to fully mimic the shoreline changes along specific coastlines. In the future, models that combine the different processes and factors contributing to shoreline change will likely allow meaningful forecasts or hindcasts of raw shoreline change patterns, including the magnitude of rates and their alongshore variations. However, such models do not yet exist—and the coastal science community is still trying to understand what causes the observed temporal and spatial variability in shoreline change rates. A simplified, “exploratory” model such as the CEM can help illuminate the component of shoreline change arising from wave climate (meaning here the angular distribution of wave influences on alongshore transport) and wave climate changes. The comparisons between model hindcasts and historical observations that we have emphasized (Figure 16) serve to test whether the signal of wave climate change is embedded in the observed shoreline change—change that results from a combination of different factors and processes. Detecting the hindcast signal of temporal shifts in alongshore patterns of shoreline change rates, as is suggested by Figure 16, indicates that this climate change effect can play a significant role in determining past—and future—shoreline changes.

5.2. Atmospheric and Oceanic Climate Shifts and Implications for the Future

Figure 17 shows the interannual variability of the yearly occurrence probability of the DWTs. We highlight in purple frequent winter low pressure systems in the North Atlantic, and we distinguish two different flavors of them in the upper panel of Figure 18: the aquamarine (wSTRONG, DWT numbers: 28, 19, 29, 37, and 38) associated with the lowest pressure systems and the pistachio green (wWEAK, DWT numbers: 10, 11, and 20) associated with very persistent and weak pressure systems, usually related with a negative phase of North Atlantic Oscillation.

According to Müller et al. (2015) in the period prior to the 1900s, the North Atlantic Oscillation state and the associated weak winds resulted in a weak North Atlantic Current and subpolar gyre, which is translated into less warm water going to the North and thus less Labrador Sea convection. This is in line with reduced probabilities found in wSTRONG and increased in wWEAK in the period before the 1910s compared with the period 1910s–1930s. From the 1910s Arctic freshwater export is reduced. Thus, the North Atlantic Current and the subpolar gyre are strengthened. The Labrador Sea convection and Atlantic Meridional Overturning Circulation increase. The intensified North Atlantic Current, subpolar gyre, and Atlantic Meridional Overturning Circulation redistribute subtropical water into the North Atlantic and Nordic Seas, therefore increasing observed and modeled temperature and salinity during the 1920s on higher latitude, which is also reflected

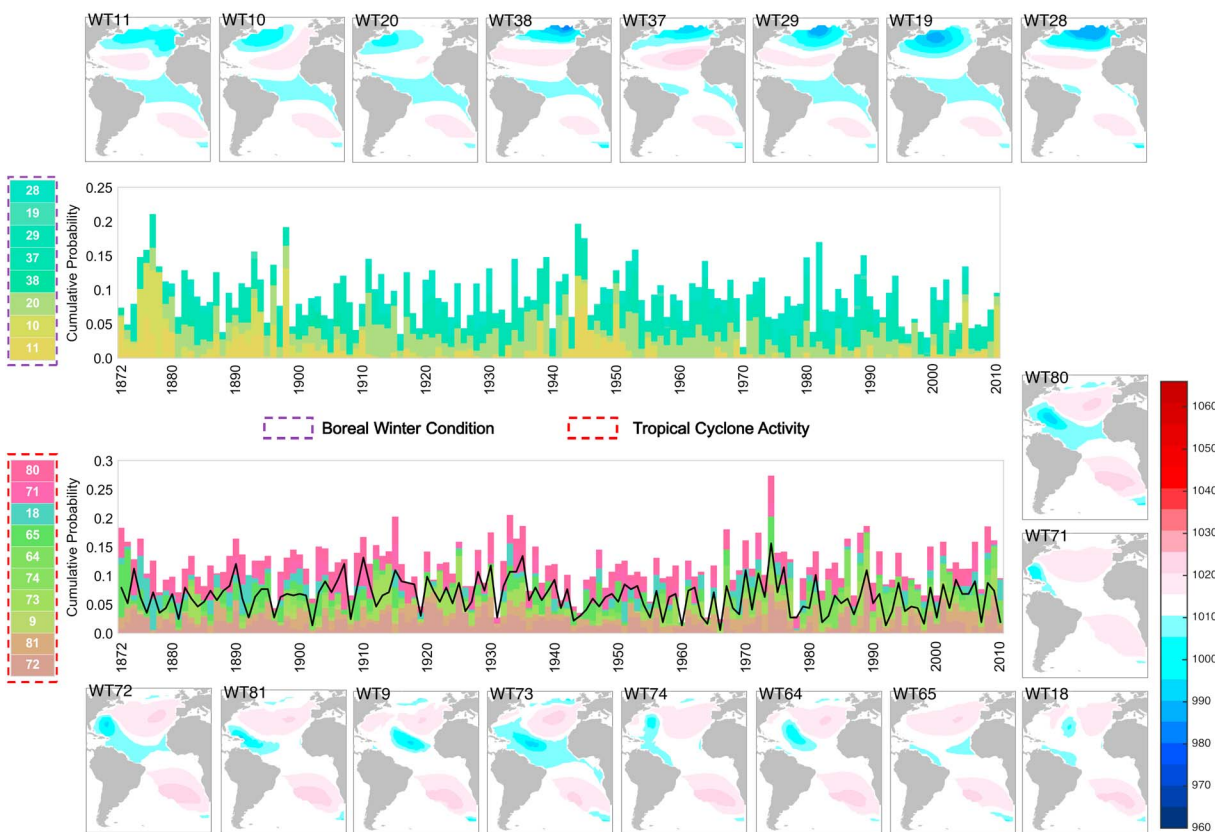


Figure 18. Interannual variability for the highlighted DWTs in Figure 17. The black line is the cumulative probability of DWTs 71, 72, 80, and 81, which are associated with TC activity near the U.S. East Coast.

in the shifts in the probabilities of wSTRONG (higher) and wWEAK (lower) for that period. Fenster and Dolan (1994) found nearly two thirds of the U.S. East Coast shorelines have undergone a significant change in the long-term rates of change between 1950s and 1980s, which could be related with the shift in the wSTRONG (higher-lower-higher) and wWEAK (lower-higher-lower) DWT probabilities during the 1930s–1970s (upper panel, Figure 18), considering some time lag in coastline responses (Thomas et al., 2016).

Changes in TC activity will also affect wave climates and coastline change patterns. The red rectangle in Figure 17 highlights weather types related to TC activity, taking place during the TC season—August–October—(see left panel of Figure 4). Moore et al. (2013) explain the dynamics of modern cusped shorelines from observed changes in hurricane-driven waves, which matches the shift in TC activity during the 1970s (lower panel, Figure 18). Peaks in the probabilities of the DWTs corresponding to TCs near the Southeastern U.S. coast also occur prior to approximately 1910, as shown in Figure 18. The Gulf Stream passes by the Southeastern U.S. coast, and the weakened flow of warm water northward prior to 1900 (Müller et al., 2015) would have caused more heat to accumulate in the coastal waters during that time. Warmer coastal water would tend to enhance tropical activity there—allowing tropical storms to retain more strength as they propagate northward, compared with other periods. One result would be that tropical storms making landfalls along the Carolina coast would tend to be stronger, compared with other periods—likely explaining why multiple strong hurricanes made landfall along the Carolina coast during this period (Stick, 1990).

The downscaled hindcasts reflect such occurrences. In the SSTs near the center of Figure 10 (rows 6 and 7 and columns 6 and 7), large magnitude contributions from waves approaching from the east and just south of east represent landfalling or near landfalling TCs, with the strongest onshore winds from these directions generating the largest waves (Moore et al., 2013). The decadal directional distributions of influences on alongshore transport in Figure 11 represents the dominant effect such landfalling or near landfalling TCs had during the 1880s and 1890s (and to a lesser degree, 1900–1910). The TC-generated waves tend to increase the asymmetry of the wave climate, *A*. They also tend to decrease *U*. (The decreased occurrences of wSTRONG noted

above, and associated decrease in waves from high angles north of east, during the pre-1900 period, would also tend to decrease U , although these effects are less striking in Figure 11.) The corresponding trends in A and U , shown in the right panel of Figure 13, drive the dramatic shifts in erosion and accretion patterns during period 1 (before 1917) shown in the middle panel of Figure 13.

This strong signal of erosion and accretion, combined with a contrasting erosion/accretion pattern during period 2 (1917–1946), produces the result in the top panel of Figure 16. The fact that the observations, as synthesized into the bottom two panels of Figure 16, qualitatively match the signal predicted in the top panel of Figure 16, despite the factors complicating the comparison (including different limits on period 1), suggests that basin-scale climate shifts produce significant responses in coastline shape. Scenarios for future basin-scale shifts in climate can be generated by global climate models. Such scenarios are likely to include the warming of coastal waters that may have contributed to the strong signal that seems clear in Figure 16. Based on the comparison in Figure 16, the downscaling procedure presented here provides the opportunity to forecast the component of the future pattern of shoreline change rates related to shifting climate states through shifts in wave climates—whether decadal-scale oscillations or a trend related to global warming.

6. Conclusions

The hybrid methodology presented here provides a computationally efficient way to downscale from ocean basin-scale meteorological climate to the nearshore wave and wind climate affecting any particular coastline. The multivariate wave and wind climate could be used to examine a range of different types of coastal responses, including the statistics of total water levels and coastal flooding. Here we use the local wave climate to investigate shifts in coastline shape. This methodology captures the interannual and interdecadal shifts in the climate forcing throughout the last century and hindcasts how these shifts may have affected coastline shape (along the coast of the Carolinas, USA, as a case study). Coastline-shape responses manifest as shifts in the patterns of shoreline change rates. An initial comparison between predicted and observed shifts in patterns of shoreline change rates suggests the conclusion that climate shifts can play a significant role in determining shoreline change rates, increasing or decreasing erosion rates by up to meters per year. This method combines statistical, data mining and dynamic modeling techniques that now are available to quickly address coastal responses to projected future climate change.

Acknowledgments

This work was partially funded by the "U.S. National Science Foundation, Coupled Natural Human Systems Program." J. A. A. Antolínez is indebted to the MEC (Ministerio de Educación, Cultura y Deporte, Spain) for the funding provided in the FPU (Formación del Profesorado Universitario) studentship (BOE-A-2013-12235). J. A. A. Antolínez and F. J. Méndez acknowledge the support of the Spanish "Ministerio de Economía y Competitividad" under grant BIA2014-59643-R. Graham Farley acknowledges the University of North Carolina at Chapel Hill and The National Science Foundation GLD Program (EAR 1324973). We thank Editor Giovanni Coco, Curt Storlazzi, and three anonymous journal reviewers for their thorough and constructive comments. NOAA-CIRES 20th Century Reanalysis (V2) and NCEP Climate Forecast System Reanalysis are provided by the NOAA/OAR/ESRL PSD, Boulder, Colorado, USA, from their Web site at <http://www.esrl.noaa.gov/psd/>. Wave data from Global Ocean Waves (GOW2) database could be requested to Environmental Hydraulics Institute at e-mail address: ihdata@ihcantabria.com.

References

- Antolínez, J. A. A., Méndez, F. J., Camus, P., Vitousek, S., González, E. M., Ruggiero, P., & Barnard, P. (2016). A multiscale climate emulator for long-term morphodynamics (MUSCLEmorpho). *Journal of Geophysical Research: Oceans*, *121*, 1–16. <https://doi.org/10.1002/2015JC011107>
- Ashton, A., Murray, A. B., & Arnoult, O. (2001). Formation of coastline features by large-scale instabilities induced by high-angle waves. *Nature*, *414*(6861), 296–300.
- Ashton, A., Murray, A. B., & Arnoult, O. (2002). Erratum: Formation of coastline features by large-scale instabilities induced by high-angle waves. *Nature*, *415*(6872), 666–666. <https://doi.org/10.1038/415666a>
- Ashton, A. D., & Murray, A. B. (2006a). High-angle wave instability and emergent shoreline shapes: 1. Modeling of sand waves, flying spits, and capes. *Journal of Geophysical Research*, *111*, F04011. <https://doi.org/10.1029/2005JF000422>
- Ashton, A. D., & Murray, A. B. (2006b). High-angle wave instability and emergent shoreline shapes: 2. Wave climate analysis and comparisons to nature. *Journal of Geophysical Research*, *111*, F04012. <https://doi.org/10.1029/2005JF000423>
- Booij, N., Ris, R. C., & Holthuijsen, L. H. (1999). A third-generation wave model for coastal regions: 1. Model description and validation. *Journal of Geophysical Research*, *104*(C4), 7649–7666. <https://doi.org/10.1029/98JC02622>
- Bruun, P. (1962). Sea-level rise as a cause of shore erosion. *Journal of the Waterways and Harbors Division*, *88*(1), 117–132.
- Camus, P., Mendez, F. J., & Medina, R. (2011). A hybrid efficient method to downscale wave climate to coastal areas. *Coastal Engineering*, *58*(9), 851–862. <https://doi.org/10.1016/j.coastaleng.2011.05.007>
- Camus, P., Mendez, F. J., Medina, R., & Cofiño, A. S. (2011). Analysis of clustering and selection algorithms for the study of multivariate wave climate. *Coastal Engineering*, *58*(6), 453–462. <https://doi.org/10.1016/j.coastaleng.2011.02.003>
- Camus, P., Méndez, F. J., Losada, I. J., Menéndez, M., Espejo, A., Pérez, J., ... Guanche, Y. (2014). A method for finding the optimal predictor indices for local wave climate conditions. *Ocean Dynamics*, *64*(7), 1025–1038. <https://doi.org/10.1007/s10236-014-0737-2>
- Camus, P., Menéndez, M., Méndez, F. J., Izaguirre, C., Espejo, A., Cánovas, V., ... Medina, R. (2014). A weather-type statistical downscaling framework for ocean wave climate. *Journal of Geophysical Research: Oceans*, *119*, 7389–7405. <https://doi.org/10.1002/2014JC010141>
- Compo, G. P., Whitaker, J. S., Sardeshmukh, P. D., Matsui, N., Allan, R. J., Yin, X., ... Worley, S. J. (2011). The twentieth century reanalysis project. *Quarterly Journal of the Royal Meteorological Society*, *137*(654), 1–28. <https://doi.org/10.1002/qj.776>
- Cowell, P. J., Stive, M. J., Niedoroda, A. W., de Vriend, H. J., Swift, D. J., Kaminsky, M., & Capobianco, G. M. (2003). The coastal-tract (Part 1): A conceptual approach to aggregated modeling of low-order coastal change. *Journal of Coastal Research*, *19*(4), 812–827.
- Cowell, P. J., Stive, M. J., Niedoroda, A. W., Swift, D. J., de Vriend, H. J., Buijsman, M. C., ... de Boer, P. L. (2003). The coastal-tract (Part 2): Applications of aggregated modeling of lower-order coastal change. *Journal of Coastal Research*, *19*(4), 828–848.
- de Vriend, H., Capobianco, M., Chesher, T., de Swart, H., Latteux, B., & Stive, M. (1993). Approaches to long-term modelling of coastal morphology: A review. *Coastal Engineering*, *21*(1–3), 225–269. [https://doi.org/10.1016/0378-3839\(93\)90051-9](https://doi.org/10.1016/0378-3839(93)90051-9)
- Falqués, A., Coco, G., & Huntley, D. A. (2000). A mechanism for the generation of wave-driven rhythmic patterns in the surf zone. *Journal of Geophysical Research*, *105*(C10), 24,087–24,971.

- Falqués, A., Ribas, F., Idier, D., & Arriaga, J. (2017). Formation mechanisms for self-organized km-scale shoreline sand waves. *Journal of Geophysical Research: Earth Surface*, 122, 1121–1138. <https://doi.org/10.1002/2016JF003964>
- Fenster, M., & Dolan, R. (1994). Large-scale reversals in shoreline trends along the U.S. mid-Atlantic coast. *Geology*, 22, 543. [https://doi.org/10.1130/0091-7613\(1994\)022<0543:LSRIST>2.3.CO;2](https://doi.org/10.1130/0091-7613(1994)022<0543:LSRIST>2.3.CO;2)
- Franke, R. (1982). Scattered data interpolation: Tests of some methods. *Mathematics of Computation*, 38(157), 181–181. <https://doi.org/10.1090/S0025-5718-1982-0637296-4>
- Fredsoe, J., & Deigaard, R. (1992). *Mechanics of coastal sediment transport*, In *Advanced Series on Ocean Engineering*, (Vol. 3). Singapore: World Scientific Publishing Co Inc.
- French, J., Payo, A., Murray, B., Orford, J., Eliot, M., & Cowell, P. (2016). Appropriate complexity for the prediction of coastal and estuarine geomorphic behaviour at decadal to centennial scales. *Geomorphology*, 256, 3–16. <https://doi.org/10.1016/j.geomorph.2015.10.005>
- Hallermeier, R. J. (1980). A profile zonation for seasonal sand beaches from wave climate. *Coastal Engineering*, 4(C), 253–277. [https://doi.org/10.1016/0378-3839\(80\)90022-8](https://doi.org/10.1016/0378-3839(80)90022-8)
- Hegermiller, C. A., Antolinez, J. A. A., Rueda, A., Camus, P., Perez, J., Erikson, L. H., ... Mendez, F. J. (2017). A multimodal wave spectrum-based approach for statistical downscaling of local wave climate. *Journal of Physical Oceanography*, 47(2), 375–386. <https://doi.org/10.1175/JPO-D-16-0191.1>
- Idier, D., Falqués, A., Ruessink, B. G., & Garnier, R. (2011). Shoreline instability under low-angle wave incidence. *Journal of Geophysical Research*, 116, F04031. <https://doi.org/10.1029/2010JF001894>
- Intergovernmental Panel on Climate Change (2013). *Climate change 2013: The physical science basis. Contribution of Working Group I to the Fifth Assessment Report of the Intergovernmental Panel on Climate Change, book section Technical Summary* (pp. 33–115). Cambridge, United Kingdom and New York: Cambridge University Press. <https://doi.org/10.1017/CBO9781107415324.005>
- Johnson, J. M., Moore, L. J., Ells, K., Murray, A. B., Adams, P. N., MacKenzie, R. A., & Jaeger, J. M. (2015). Recent shifts in coastline change and shoreline stabilization linked to storm climate change. *Earth Surface Processes and Landforms*, 40(5), 569–585. <https://doi.org/10.1002/esp.3650>
- Kaergaard, K., & Fredsoe, J. (2013a). Numerical modeling of shoreline undulations Part 1: Constant wave climate. *Coastal Engineering*, 75, 64–76. <https://doi.org/10.1016/j.coastaleng.2012.11.006>
- Kaergaard, K., & Fredsoe, J. (2013b). Numerical modeling of shoreline undulations Part 2: Varying wave climate and comparison with observations. *Coastal Engineering*, 75, 77–90. <https://doi.org/10.1016/j.coastaleng.2012.11.003>
- Kinsela, M. A., & Cowell, P. J. (2015). Controls on shoreface response to sea level change. In P. Wang, J. D. Rosati, & J. Cheng (Eds.), *Coastal sediments* (Chap. 204, Vol. 2015). Singapore: World Scientific Publishing Co Pte Ltd.
- Komar, P. D. (1971). The mechanics of sand transport on beaches. *Journal of Geophysical Research*, 76(3), 713–721. <https://doi.org/10.1029/JC076i003p00713>
- Komar, P. D., & Allan, J. C. (2008). Increasing hurricane-generated wave heights along the U.S. East Coast and their climate controls. *Journal of Coastal Research*, 24(2), 479–488. <https://doi.org/10.2112/07-0894.1>
- Lazarus, E. D., & Murray, A. B. (2007). Process signatures in regional patterns of shoreline change on annual to decadal time scales. *Geophysical Research Letters*, 34, L19402. <https://doi.org/10.1029/2007GL031047>
- Limber, P. W., Adams, P. N., & Murray, A. B. (2017). Modeling large-scale shoreline change caused by complex bathymetry in low-angle wave climates. *Marine Geology*, 383, 55–64. <https://doi.org/10.1016/j.margeo.2016.11.006>
- McNinch, J. E. (2004). Geologic control in the nearshore: Shore-oblique sandbars and shoreline erosional hotspots, Mid-Atlantic Bight, USA. *Marine Geology*, 211(1), 121–141. <https://doi.org/10.1016/j.margeo.2004.07.006>
- Méndez, F. J., Menéndez, M., Luceño, A., & Losada, I. J. (2007). Analyzing monthly extreme sea levels with a time-dependent GEV model. *Journal of Atmospheric and Oceanic Technology*, 24(5), 894–911. <https://doi.org/10.1175/JTECH2009.1>
- Moore, L. J., List, J. H., Williams, S. J., & Stolper, D. (2010). Complexities in barrier island response to sea level rise: Insights from numerical model experiments, North Carolina Outer Banks. *Journal of Geophysical Research*, 115, F03004. <https://doi.org/10.1029/2009JF001299>
- Moore, L. J., McNamara, D. E., Murray, A. B., & Brenner, O. (2013). Observed changes in hurricane-driven waves explain the dynamics of modern cusped shorelines. *Geophysical Research Letters*, 40, 5867–5871. <https://doi.org/10.1002/2013GL057311>
- Morton, R. A., & Miller, T. L. (2005). The national assessment of shoreline change: Part 2, Historical shoreline changes and associated coastal land loss along the U.S. Southeast Atlantic Coast, U.S. Geological Survey Open File Report 2005-1401.
- Müller, W. A., Matei, D., Bersch, M., Jungclaus, J. H., Haak, H., Lohmann, K., ... Marotzke, J. (2015). A twentieth-century reanalysis forced ocean model to reconstruct the North Atlantic climate variation during the 1920s. *Climate Dynamics*, 44(7), 1935–1955. Retrieved from <https://doi.org/10.1007/s00382-014-2267-5>
- Murray, A. B. (2007). Reducing model complexity for explanation and prediction. *Geomorphology*, 90(3–4), 178–191. <https://doi.org/10.1016/j.geomorph.2006.10.020>
- Murray, A. B., & Ashton, A. D. (2013). Instability and finite-amplitude self-organization of large-scale coastline shapes. *Philosophical Transactions of the Royal Society of London A: Mathematical, Physical and Engineering Sciences*, 371(2004), 20120363. <https://doi.org/10.1098/rsta.2012.0363>
- National Oceanic and Atmospheric Administration, NOAA (2012). National Geodetic Survey NOAA Shoreline Data Explorer. Retrieved from http://www.ngs.noaa.gov/newsys_ims/shoreline/index.cfm
- Nicholls, R. J., & Cazenave, A. (2010). Sea level rise and its impact on coastal zones. *Science*, 328(2010), 1517–1520. <https://doi.org/10.1126/science.1185782>
- Pérez, J., Méndez, F. J., Menéndez, M., & Losada, I. J. (2014). ESTELA: a method for evaluating the source and travel time of the wave energy reaching a local area. *Ocean Dynamics*, 64(8), 1181–1191. <https://doi.org/10.1007/s10236-014-0740-7>
- Perez, J., Menendez, M., & Losada, I. J. (2017). GOW2: A global wave hindcast for coastal applications. *Coastal Engineering*, 124, 1–11. <https://doi.org/10.1016/j.coastaleng.2017.03.005>
- Perez, J., Menendez, M., Camus, P., Mendez, F. J., & Losada, I. J. (2015). Statistical multi-model climate projections of surface ocean waves in Europe. *Ocean Modelling*, 96(Part 1), 161–170. <https://doi.org/10.1016/j.ocemod.2015.06.001>
- Rippa, S. (1999). An algorithm for selecting a good value for the parameter c in radial basis function interpolation. *Advances in Computational Mathematics*, 11, 193–210. <https://doi.org/10.1023/A:1018975909870>
- Robinet, A., Castelle, B., Idier, D., Le Cozannet, G., Déqué, M., & Charles, E. (2016). Statistical modeling of interannual shoreline change driven by North Atlantic climate variability spanning 2000–2014 in the Bay of Biscay. *Geo-Marine Letters*, 36(6), 479–490. <https://doi.org/10.1007/s00367-016-0460-8>
- Rueda, A., Hegermiller, C. A., Antolinez, J. A. A., Camus, P., Vitousek, S., Ruggiero, P., ... Mendez, F. J. (2017). Multiscale climate emulator of multimodal wave spectra: MUSCLE-spectra. *Journal of Geophysical Research: Oceans*, 122, 1400–1415. <https://doi.org/10.1002/2016JC011957>

- Saha, S., Moorthi, S., Pan, H. L., Wu, X., Wang, J., Nadiga, S., . . . Goldberg, M. (2010). The NCEP climate forecast system reanalysis. *Bulletin of the American Meteorological Society*, *91*(8), 1015–1057. <https://doi.org/10.1175/2010BAMS3001.1>
- Schupp, C. A., McNinch, J. E., & List, J. H. (2006). Nearshore shore-oblique bars, gravel outcrops, and their correlation to shoreline change. *Marine Geology*, *233*(1), 63–79. <https://doi.org/10.1016/j.margeo.2006.08.007>
- Slott, J. M., Murray, A. B., Ashton, A. D., & Crowley, T. J. (2006). Coastline responses to changing storm patterns. *Geophysical Research Letters*, *33*, L18404. <https://doi.org/10.1029/2006GL027445>
- Stick, D. (1990). *The Outer Banks of North Carolina, 1584–1958* (p. 367). Chapel Hill: University of North Carolina Press.
- Stive, M. J. F. (2004). How important is global warming for coastal erosion. *Climatic Change*, *64*(1–2), 27–39. <https://doi.org/10.1023/B:CLIM.0000024785.91858.1d>
- Thomas, C. W., Murray, A. B., Ashton, A. D., Hurst, M. D., Barkwith, A. K., & Ellis, M. A. (2016). Complex coastlines responding to climate change: do shoreline shapes reflect present forcing or “remember” the distant past? *Earth Surface Dynamics*, *4*(4), 871–884.
- United States Geological Survey, USGS (2011). The national assessment of shoreline change: A GIS compilation of vector shorelines and associated shoreline change data for the U.S. Southeast Atlantic Coast. [Data file: nc_zip], Retrieved from <http://pubs.usgs.gov/of/2005/1326/gis-data.html>
- Valvo, L. M., Murray, A. B., & Ashton, A. (2006). How does underlying geology affect coastline change? An initial modeling investigation. *Journal of Geophysical Research*, *111*, F02025. <https://doi.org/10.1029/2005JF000340>
- Weatherall, P., Marks, K. M., Jakobsson, M., Schmitt, T., Tani, S., Arndt, J. E., . . . Wigley, R. (2015). A new digital bathymetric model of the world's oceans. *Earth and Space Science*, *2*, 331–345. <https://doi.org/10.1002/2015EA000107>
- Wolinsky, M. A., & Murray, A. B. (2009). A unifying framework for shoreline migration: 2. Application to wave-dominated coasts. *Journal of Geophysical Research*, *114*, F01009. <https://doi.org/10.1029/2007JF000856>